iScience

CellPress

Article

Geometry-Dependent Spectroscopic Contrast in Deep Tissues

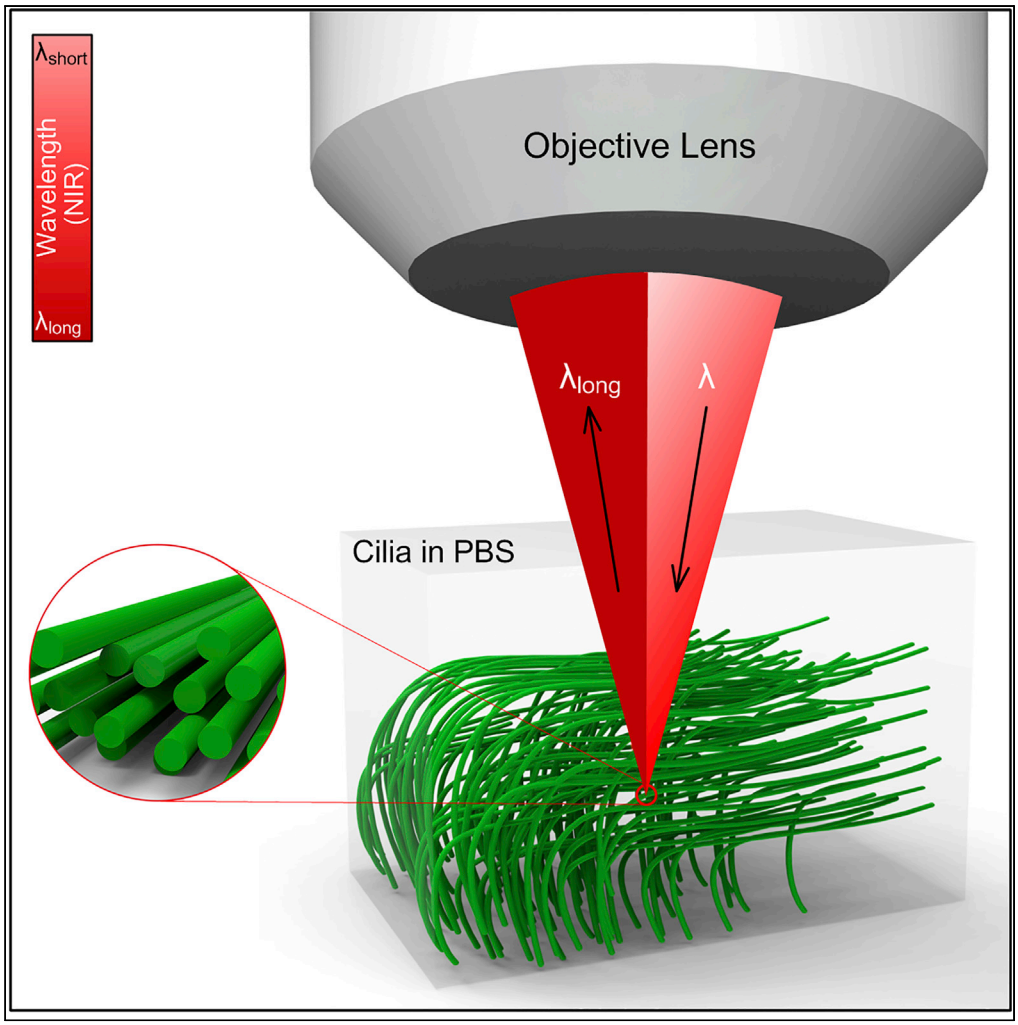

Xin Ge, Hongying Tang, Xianghong Wang, ..., Steven M. Rowe, Guillermo J. Tearney, Linbo Liu

smrowe@uab.edu (S.M.R.)
gtearney@partners.org (G.J.T.)
liulinbo@ntu.edu.sg (L.L.)

HIGHLIGHTS

Long-wavelength shifts of packed nano-cylinders in the backscattered NIR spectra

Experimental observations of characterized spectroscopic contrast in deep tissue

Physics behind is described by an analytical model using the radial distribution function

Spectroscopic contrast of fibrous structures is sensitive to the external pressure

Ge et al., iScience *19*, 965–975
September 27, 2019
https://doi.org/10.1016/j.isci.2019.08.046

iScience

CellPress

Article

Geometry-Dependent Spectroscopic Contrast in Deep Tissues

Xin Ge,[1,11] Hongying Tang,[2,11] Xianghong Wang,[1,11] Xinyu Liu,[1] Si Chen,[1] Nanshuo Wang,[1] Guangming Ni,[3] Xiaojun Yu,[4] Shufen Chen,[1] Haitao Liang,[1] En Bo,[1] Lulu Wang,[1] Cilwyn Shalitha Braganza,[1] Chenjie Xu,[5] Steven M. Rowe,[6,7,*] Guillermo J. Tearney,[8,9,10,*] and Linbo Liu[1,5,12,*]

SUMMARY

Nano-structures of biological systems can produce diverse spectroscopic effects through interactions with broadband light. Although structured coloration at the surface has been extensively studied, natural spectroscopic contrasts in deep tissues are poorly understood, which may carry valuable information for evaluating the anatomy and function of biological systems. Here we investigated the spectroscopic characteristics of an important geometry in deep tissues at the nanometer scale: packed nano-cylinders, in the near-infrared window, numerically predicted and experimentally proved that transversely oriented and regularly arranged nano-cylinders could selectively backscatter light of the long wavelengths. Notably, we found that the spectroscopic contrast of nanoscale fibrous structures was sensitive to the pressure load, possibly owing to the changes in the orientation, the degree of alignment, and the spacing. To explore the underlying physical basis, we further developed an analytical model based on the radial distribution function in terms of their radius, refractive index, and spatial distribution.

INTRODUCTION

In contrast to that produced by selective absorption, the spectral modulation of light reflected or scattered by a non-luminous object is mainly due to elastic interactions between the input light and micro- and nano-structures. This spectral modulation may bring about spectroscopic contrasts manifested as spectral centroid shifts in the back-scattered light fields. Since Robert Hooke and Isaac Newton revealed the basis of structural coloration (Hooke, 1665; Newton, 1704), fascinating colors created by natural structures have attracted considerable research interests (Vukusic and Sambles, 2003; Wiersma, 2013). In biology, structural colors are commonly observed under sunlight or white light on the surfaces of animals and plants (Cuthill et al., 2017; Moyroud et al., 2017; Teyssier et al., 2015; Vignolini et al., 2012) (skin, feathers, flowers, and epicarp). However, as turbid tissues are opaque to visible light, the direct observation of structural colors originating from beneath biological tissues is extremely difficult.

The spectroscopic properties of deep biological tissues are commonly investigated within the near-infrared (NIR) window (650–1,350 nm), where the light has its maximum penetration. For more than a decade, an NIR reflectance microscopic technique termed spectroscopic optical coherence tomography (SOCT) has been developed (Leitgeb et al., 2000; Morgner et al., 2000; Oldenburg et al., 2007; Xu et al., 2006). SOCT detects the light signals from a micrometer-scale sample volume while rejecting the light from the background, a unique capability known as optical sectioning, which makes it possible to probe microstructures through 1- to 2-mm opaque tissues. The effect of scatterer size on the back-scattered spectra has led to the use of SOCT to evaluate the cell nuclei (Robles and Wax, 2010; Robles et al., 2010; Wax et al., 2011; Xu et al., 2005) and probe nanoscale information (Azarin et al., 2015; Yi et al., 2013). The spectra of random microspheres packing have been investigated extensively (Tseng et al., 2006); detailed understanding of nanoscale shape on spectroscopic contrast, however, remains elusive.

At the nanometer level, the two fundamental geometries of biological tissues are spherical geometry, such as mitochondria and various intracellular granules, and cylindrical geometry, such as motile cilia, collagen fibrils, and elastic fibers. It is intriguing to know how different nanoscale geometries may alter the spectrum of scattered light and whether it is possible to extract biologically relevant information from their spectroscopic signatures. The answers to these questions are pertinent to a variety of clinical and scientific research fields where optical reflectance imaging techniques are widely used, such as noninvasive

[1]School of Electrical and Electronic Engineering, Nanyang Technological University, Singapore 639798, Republic of Singapore

[2]College of Information, Mechanical and Electrical Engineering, Shanghai Normal University, Shanghai 200234, China

[3]School of Optoelectronic Science and Engineering, University of Electronic Science and Technology of China, Chengdu 610054, China

[4]School of Automation, Northwestern Polytechnical University, Xi'an, Shaanxi 710072, China

[5]School of Chemical and Biomedical Engineering, Nanyang Technological University, Singapore 637459, Republic of Singapore

[6]Gregory Fleming James Cystic Fibrosis Research Center, University of Alabama at Birmingham, Birmingham, AL 35294, USA

[7]Department of Medicine, University of Alabama at Birmingham, Birmingham, AL 35294, USA

[8]Wellman Center for Photomedicine, Harvard Medical School and Massachusetts General Hospital, Boston, MA 02114, USA

[9]Harvard-MIT Division of Health Sciences and Technology, Cambridge, MA 02139, USA

[10]Department of Pathology, Harvard Medical School and Massachusetts General Hospital, Boston, MA 02114, USA

[11]These authors contributed equally

[12]Lead Contact

Continued

anatomical and functional imaging of microstructures in the respiratory mucosa, the blood vessel wall, the posterior segment of the eye, the skin, and the gastrointestinal mucosa (Fujimoto, 2003; Huang et al., 1991; Liu et al., 2011; Tearney et al., 1997; Yelin et al., 2006; Yun et al., 2006), nanoscale mapping of nuclear architecture (Uttam et al., 2015; Wang et al., 2010), or changing of partial wave spectroscopy signals by chromosome condensation (Kim et al., 2011). In this study, we established numerical models of nano-spheres and nano-cylinders and discovered that transversely oriented and regularly arranged nano-cylindrical scatterers are more likely to generate spectral centroid shifts toward the long wavelengths within the spectral window of 700–950 nm than nano-spheres, which tend to exhibit shifts toward the short end. Using a form of SOCT that operates in 700–950 nm, we verified the above-mentioned predictions on a variety of natural nano-cylindrical structures, such as motile cilia and extracellular matrix containing nanoscale fibrous structures, which exhibited a striking and consistent spectroscopic contrast against the surrounding background tissues. To our knowledge, this study is the first to demonstrate geometry-dependent spectroscopic contrasts from nanometer-scale features in deep mammalian tissues *in situ* and *in vivo*. Interestingly, we additionally found that this geometry-dependent spectroscopic contrast is sensitive to external stress, probably due to the changes in the orientation, degree of alignment, and spacing of the nano-cylinders.

RESULTS

We generated numerical models of packed nano-spheres and nano-cylinders in a micrometer-scale focal volume using the finite-difference time-domain (FDTD) method and compared their backscattered spectra detected by a single mode pinhole (Figure 1A). The details on generating packed scatterers and the computational imaging model are described in the Transparent Methods. Our SOCT system obtains cross-sectional images at a rate of up to 60 frames per second, enabling acquisition of three-dimensional (3D) images of biological tissues *in situ* and *in vivo*. The spatial resolution of the intensity image is 1.80 μm × 1.80 μm × 1.28 μm (*x*, *y*, *z*) in tissue, which allowed us to identify microscopic anatomic details to match SOCT images with corresponding histology.

Motile Cilia

The motile cilia that line the surface of mammalian respiratory airways, brain ventricles, and fallopian tubes are regularly arranged nano-cylinders. Those in the respiratory airways are ideal samples for our study because they are surrounded by aqueous periciliary liquid in a consistent mucin gel instead of an optically heterogeneous matrix with unknown optical properties (Barrick et al., 2016; Liu et al., 2013; Oldenburg et al., 2012; Sanderson and Sleigh, 1981). According to the electron microscope and digital high-speed imaging studies (Chilvers and O'callaghan, 2000; Sanderson and Sleigh, 1981), at the recovery stroke the motile cilia bend so that the apical portions of cilia are approximately parallel to the cell surface (Figure 1A), whereas at the midpoint of the effective (or power) stroke they are almost straight and perpendicular to the cell surface and stand up above those in the recovery stroke. Therefore, in optical coherence tomography (OCT) images, the scattered signals within 3–5 μm from the apical cell surface are mostly from the cilia in the recovery stroke, whereas those signals within 5–7 μm from the apical cell surface originate from the cilia tips in the effective stroke (Sanderson and Sleigh, 1981).

In our numerical model, we first considered those in the recovery stroke when the closely packed apical portions of the cilia are parallel to the airway surface and perpendicular to the input light beam (Figure 1A and Table S1) (Liu et al., 2013; Sanderson and Sleigh, 1981). The backscattered spectra of 10 groups of packed cylinders mimicking motile cilia exhibit spectral centroid shifts of 23.7 ± 26.6 nm (mean ± SD) toward the long wavelengths (Figures 1B and S1). In contrast, those from spherical scatterers with the same refractive index, diameter, and spatial arrangements tend to shift 16.9 ± 28.7 nm toward the short wavelengths (Figure 1C). Second, we considered those in the effective stroke when the orientation of the cilia varies within 0°–60° to the input beam. Our model predicted that the spectral centroid is more likely to shift toward the short wavelengths during the effective stroke (Figure S2).

We imaged normal ciliated primary human bronchial epithelial (HBE) cultures *in vitro* and intact sheep trachea *ex vivo* with functional mucociliary transport using SOCT along the direction of the effective stroke or the mucus transport. The intensity image captured the cross-sectional micro-anatomy of the mucociliary apparatus, including the airway surface liquid (phosphate-buffered saline in the cell culture), cilia, and cell bodies (Figures 2A and 2D). In the cell cultures with mucus replaced by phosphate-buffered saline, cilia in the recovery stroke and cilia in the effective stroke could be clearly differentiated (Figure 2A and Video S1). To visualize the contrast of the spectral centroid shift, we mapped it to grayscale and produced an

*Correspondence:
smrowe@uab.edu (S.M.R.),
gtearney@partners.org
(G.J.T.),
liulinbo@ntu.edu.sg (L.L.)

https://doi.org/10.1016/j.isci.2019.08.046

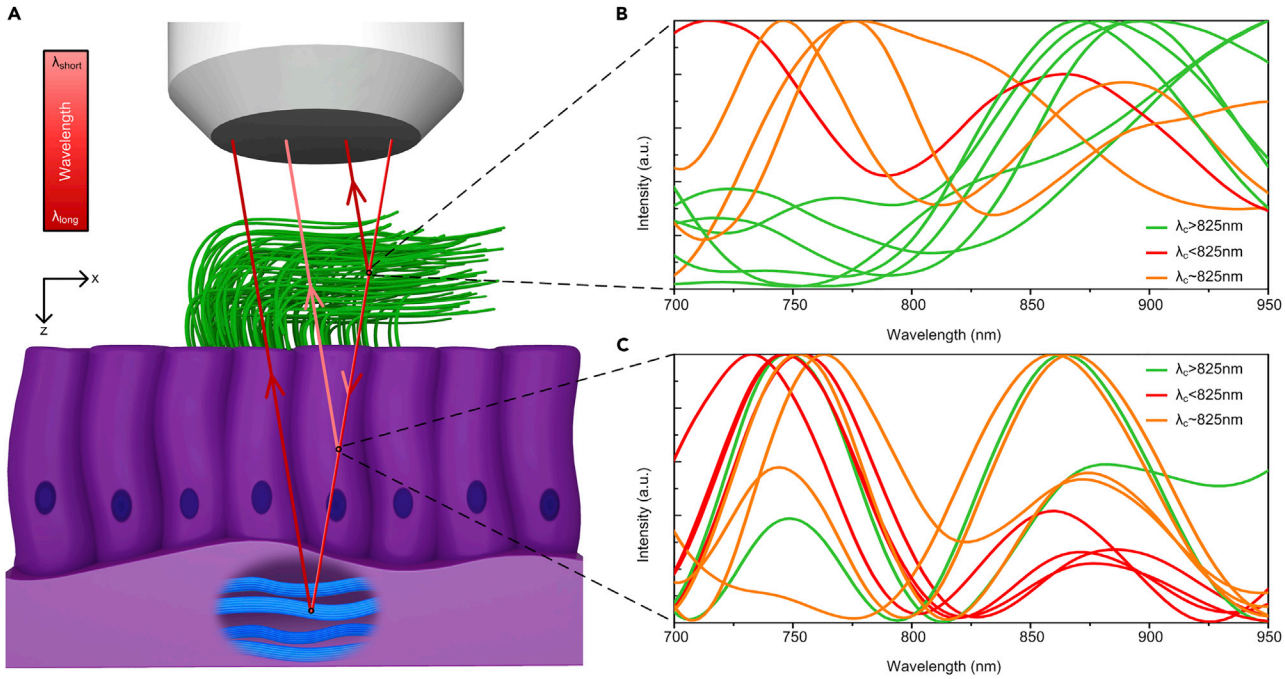

Figure 1. FDTD Simulation Reveals Characteristic Spectroscopic Contrast of Motile Cilia

(A) Schematic of light-tissue interactions in the respiratory mucosa. Color bar: light red and dark red color stand for short and long wavelengths in 700–950 nm, respectively.

(B) Backscattered spectra of transversely oriented and regularly arranged nano-cylinders simulating the apical portions of motile cilia at the recovery stroke. These transversely oriented and regularly arranged nano-cylinders were generated by the same strategy but the different seeds.

(C) Backscattered spectra of nano-spheres of the same diameter and refractive index as the cylinders in (B). Each curve in (B) and (C) was normalized to its maximum intensity. Curves with the spectral centroid shift toward the long wavelengths and short wavelengths were denoted with green and red color, respectively. Those without significant shift were denoted with orange color. λ_c is the center of gravity of the backscattered spectrum, and 825 nm is the center of gravity of the input light spectrum.

image we term the spectral centroid shift image (Figures 2B and 2E). In the cell cultures, we observed a mean spectral centroid shift of 20.4 $\pm$ 6.3 nm toward the long wavelengths in the back-scattered signals from regions consisting predominantly of cilia in the recovery stroke, whereas the mean spectral centroid shift of signals predominantly from HBE cell bodies, presumably containing more spherical scatterers, shifted 3.3 $\pm$ 7.0 nm toward the short wavelengths (Figure 2B and inset). In addition, signals from the effective stroke exhibited a spectral centroid shift of 1.5 $\pm$ 8.4 nm toward the short wavelengths (Figure 2B and inset), which is significantly different from that of the recovery stroke (paired signals from the recovery and effective stroke in 50 ciliated cells, $p < 0.001$ at the 0.05 level, Student's t test). These observations agree with our predictions shown in Figure 1. We also generated a color image, termed SOCT image, by combining the spectral centroid shift (Hue) and the intensity image (Value) using the Hue-Saturation-Value (HSV) color scheme, in which the cilia in the recovery stroke appeared as greenish structures, distinct from the reddish effective stroke and epithelial cell body (Figure 2C). In the cultured full-thickness sheep tracheal mucosa, we could also detect the same spectroscopic contrast as the HBE culture (Figures 2E and 2F). Interestingly, the lamina propria of the sheep trachea demonstrates long-wavelength shifts suggesting spectroscopic contrasts from nanofibrous structures in the extracellular matrices (Figures 2E and 2F).

Nanoscale Fibrous Structures in Extracellular Matrix

Fibrous structures in the extracellular matrix also assume the cylindrical geometry at the nanometer scale. For initial verification, we established our numerical model (Table S2) based on the collagen fibril organization in the lamina cribrosa and peripapillary sclera since they are simple in geometrical composition: their dry matter is mainly composed of transversely oriented collagen fibrils with respect to the input beam (Komai and Ushiki, 1991; Quigley et al., 1991). Similar to those from motile cilia, the backscattered spectra of 10

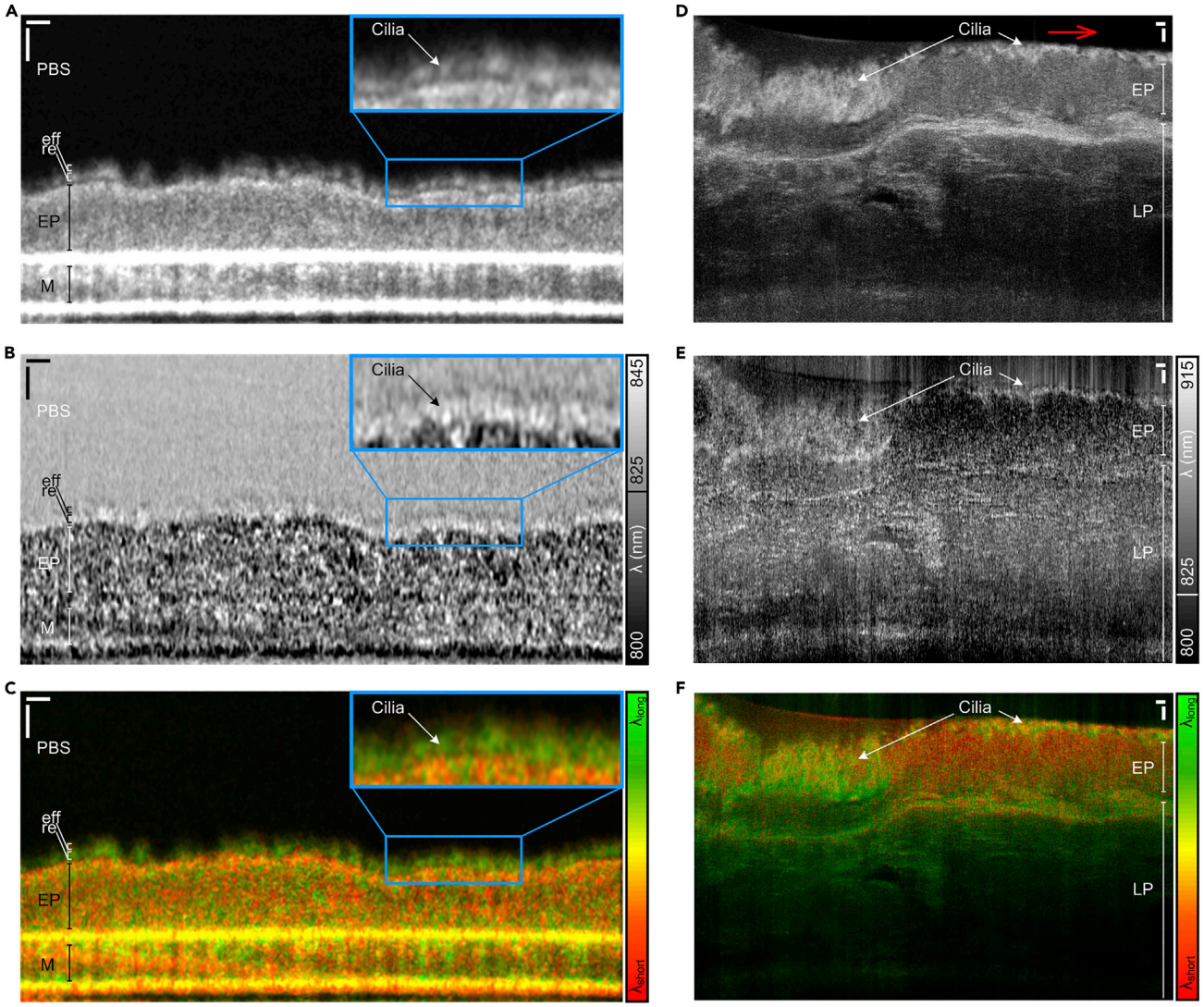

Figure 2. Geometry-Dependent Spectroscopic Contrast Images of Motile Cilia *In Vitro* and *In Vivo*

(A) A representative OCT intensity image of motile cilia in HBE culture.

(B) The corresponding spectral centroid shift image.

(C) The corresponding HSV-mapped SOCT image. PBS, phosphate-buffered saline; EP, human bronchial epithelial monolayer; M, membrane of the Transwell insert; eff, effective stroke; re, recovery stroke.

(D) A representative OCT intensity image of cultured sheep tracheal mucosa with functional mucociliary clearance *in situ*. Red arrow stands for the direction of the effective stroke. Note that the epithelium folded in the left side, so that the epithelial surface was parallel to the image plane, which "cut" through motile cilia perpendicularly. The 3D spatial relation between the image plane and the folded epithelium is explained in Figures S3B and S3C. (E) and (F) The corresponding spectral centroid shift image and HSV-mapped SOCT image, respectively. EP, epithelium; LP, lamina propria; M, mucus flow. The mark at 825 nm in the gray scale bars refers to the centroid of the input spectrum. The green hue indicates the long-wavelength shift in NIR, whereas the red hue represents shifts toward the short wavelength for all HSV-mapped images in this paper. Scale bars: 10 μm.

groups of packed cylinders mimicking collagen fibrils exhibit spectral centroid shift of 8.5 ± 8.1 nm (mean ± SD) toward the long wavelengths (Figure 3A). In contrast, those in mis-aligned configurations (assigning a random rotation angle around the z axis in [-π, π]) tend to be neutral in spectral centroid shift (Figure 3B). To validate the theoretical prediction, we acquired 3D images of the optic nerve head of freshly enucleated unpressurized swine eyes *ex vivo* (Figure 3C). Similar to motile cilia, they exhibited strong spectral centroid shifts toward the long wavelengths, whereas the prelamina region and blood vessel remained neutral or exhibited moderate shifts toward the short end (Figures 3D and 3E and Video S2). The SOCT image provides a color contrast similar to the histology image (Figure 3F).

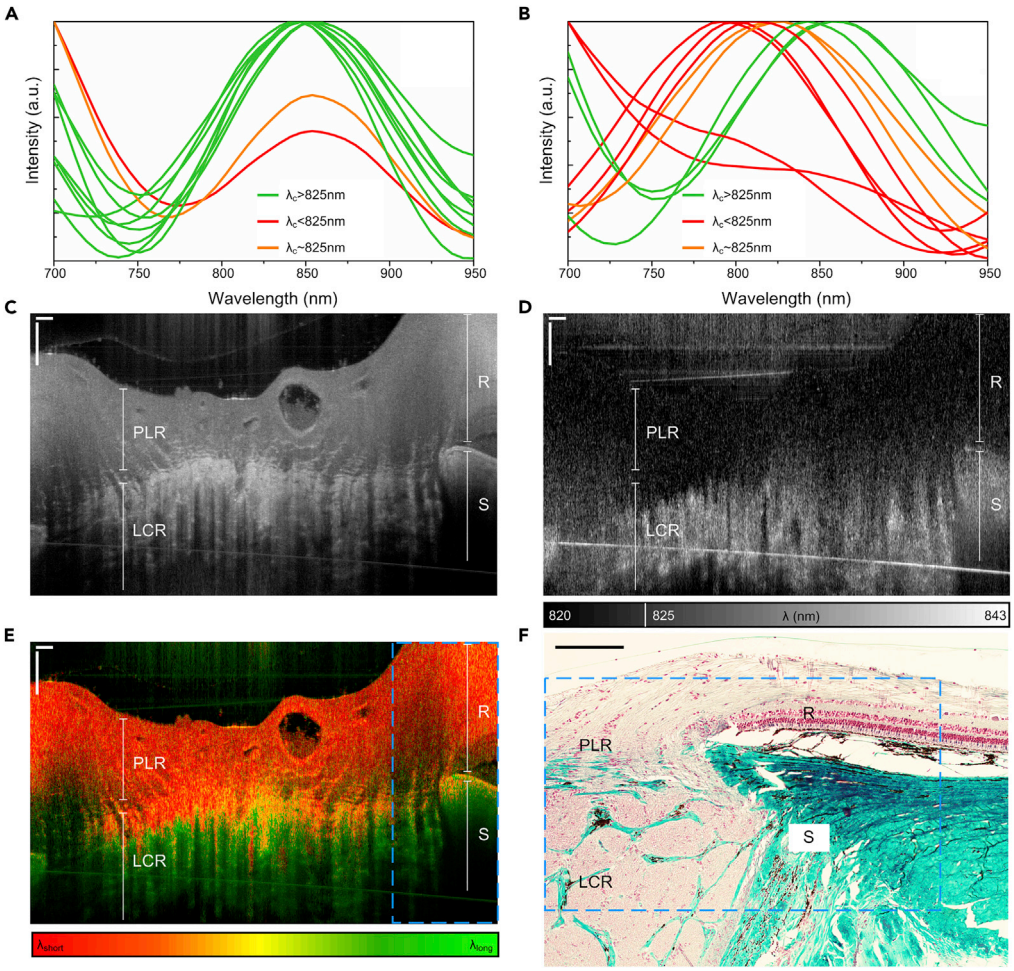

Figure 3. Geometry-Dependent Spectroscopic Scattering of Collagen Fibrils

(A) FDTD predictions of backscattered spectra from densely packed well-aligned nano-cylinders simulating collagen fibrils in lamina cribrosa and sclera.

(B) Backscattered spectra from mis-aligned nano-cylinders with the same diameter and refractive index as those in (A). Each spectrum was from a distinct spatial arrangement of cylinders generated using the same strategy.

(C) A representative intensity cross-sectional image of swine optic nerve head.

(D–F) Corresponding spectral centroid shift image (D), HSV-mapped SOCT image (E), and Masson's trichrome stained histology image (F), respectively. The spectroscopic artifacts at the top of (D) and (E) were the ghost image due to the autocorrelation artifacts of OCT signal. The cyan dashed boxes in (E) and (F) refer to the same region. LCR, lamina cribrosa; S, sclera; R, retina; PLR, prelaminar region; R, retina.

Scale bars: 100 μm.

We additionally acquired 3D images of fully expanded human skin *in vivo*, as well as fully expanded swine esophageal mucosa *in vivo*. The scatterers in the epidermis (Video S3, and Figure S4) and esophageal epithelium (Figure S5), which presumably contain more microscopic spheres, scattered more light of the short wavelengths than the long wavelengths. Although the compositions of the dermis of human skin and the lamina propria of swine esophageal mucosa are complex, there are abundant aligned nanoscale fibrous structures such as collagen fibrils and elastic fibers. The signals from the reticular dermis (Figures S4D–S4F) and esophageal lamina propria (Figure S5B) exhibited strong spectral centroid shifts toward the long wavelengths, presumably from nanoscale fibrous structures. It is noticed that the keratinized layer of swine esophageal epithelium presented spectral centroid shifts toward the long wavelengths, which was possibly generated by the well-aligned tonofilaments. Of note, in the NIR range, the absorption of water and major chromophores might have contributed to the spectroscopic contrast. However, the results from skin of different phenotypes (Figure S4) do not support a significant contribution from melanin.

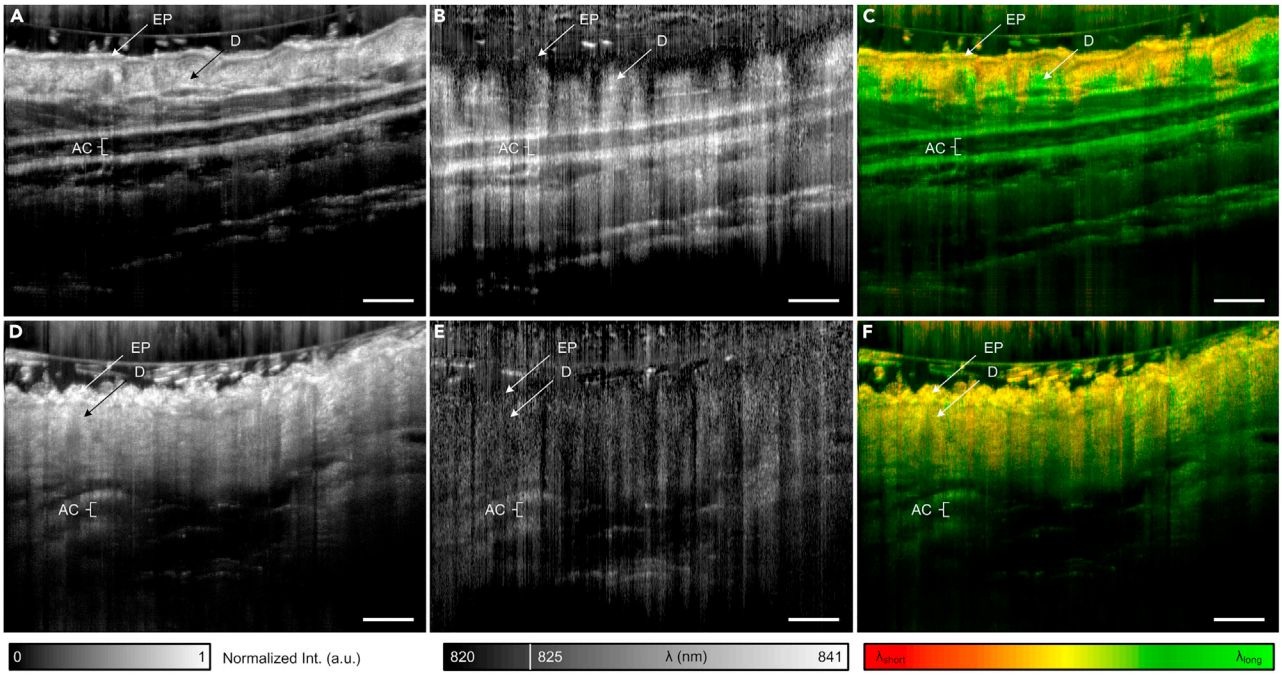

Figure 4. Geometry-Dependent Spectroscopic Contrast Is Negated by Thermal Denaturing of Collagen Fibrils *Ex Vivo*

(A–F) (A–C) are the representative intensity image, spectral centroid shift image, and HSV-mapped SOCT image from the normal control mouse ear, respectively, whereas (D–F) are those of the burned mouse ear, respectively. EP, epidermis; D, dermis; AC, auricular cartilage. Scale bars: 100 μm.

Thermal Denature of Collagen

The fact that collagen fibrils and fibers denature at high temperature (Abdullahi et al., 2014) provides a convenient model to confirm the geometry dependency of the spectroscopic contrast. To do so, we evaluated the spectroscopic signals from normal and burned ear skin of C57BL/6 mice *ex vivo* (Figure 4). Although there was no significant change in the intensity of the dermis caused by the thermal damage, the spectral centroid shift in the dermis and the articular cartilage was remarkably reduced in the burned sample (Figures 4E and 4F) compared with that of the normal control (Figures 4B and 4C), presumably due to the thermal damage in the nano-cylindrical structures.

Stress-Induced Reorganization of Nanoscale Fibers

The above-mentioned static results may provide insights into spectroscopic phenomenon in varieties of complex biological tissues and processes. The following dynamic example is related with the tunica media of the coronary wall, where thin (actin) and thick (myosin) contractile filaments in the smooth muscle cells are stretched and elastic fibers uncoil as the vessel wall expands (Dingemans et al., 2000). When we loaded the coronary artery of a fresh swine heart with a linearly increasing static phosphate-buffered saline pressure from 44.1 to 117.7 mmHg over 10 s *ex vivo*, the mean spectral centroid shift of the tunica media increased by 14.3 nm toward the long wavelengths (Figures 5A–5D, and blue line in Figure 5E). Clearly, in this dynamic process the spectral centroid shift closely followed the change of the media thickness (red line in Figure 5E), which was correlated with the intracoronary pressure change. Therefore, it is reasonable to attribute the spectral curve shifts (Figure 5F) to the reorganization of the nano-cylinder assembly, which might undergo a transition from a loose and randomly orientated morphology to a straighter, more transversely oriented and more compact morphology with a higher degree of alignment due to the external load (Yang et al., 2015). Interestingly, the fibrous pericardium (FP) fused with the serous pericardium (SP) (Figures 5A and 5B) could be easily distinguished by the spectroscopic contrast of layers of fibrils and elastin fibers in the FP (Figures 5C and 5D).

DISCUSSION

Nanometer-scale fibrous structures are ubiquitous in nature. Although their cylindrical geometry is designed to fulfill particular biological functions, it also possesses a unique wavelength-selective

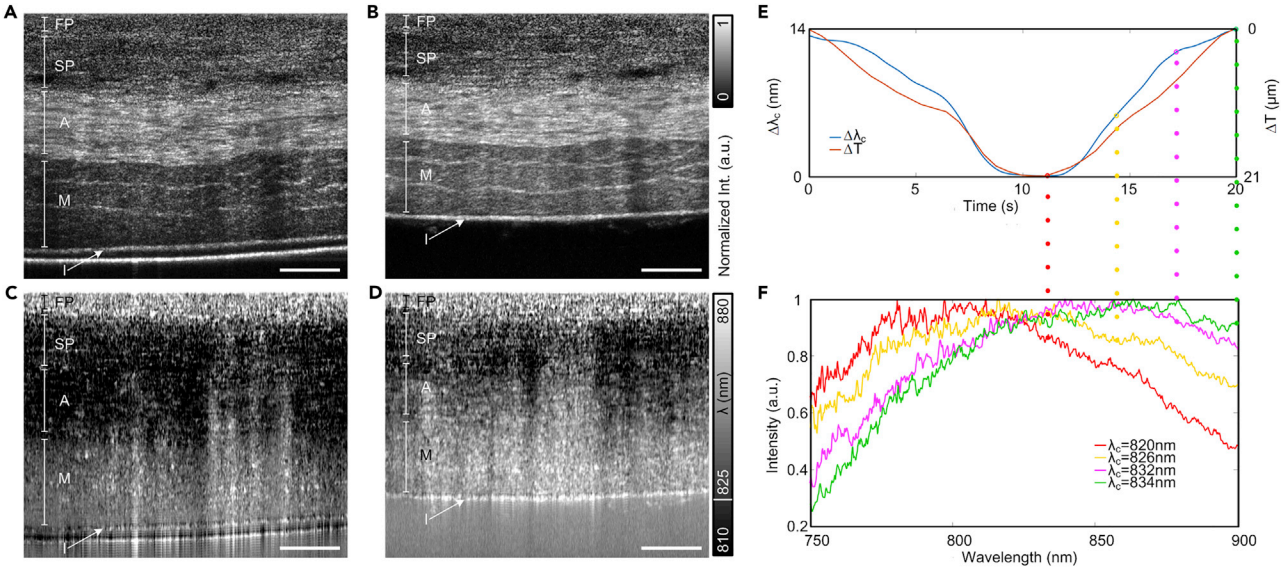

Figure 5. Changes of the Spectroscopic Contrast of the Swine Coronary Arterial Wall during Pressure Loading

(A) Representative cross-sectional intensity image acquired through the pericardium at the intracoronary hydrostatic pressure of 44.1 mm Hg. (B) Intensity image acquired in the same spot at the intracoronary hydrostatic pressure of 117.7 mm Hg. The bright interface at the bottom in (A) was from the lower surface of an air bubble, which moved out of the recorded view in (B) at high pressure (Video S4).

(C) Spectral centroid shift image corresponding to (A). (D) Spectral centroid shift image corresponding to (B). FP, fibrous pericardium; SP, serous pericardium; A, adventitia; M, media; I, intima. Scale bars: 100 μm.

(E) Dynamic correlation between the relative spectral centroid shift of the tunica media (blue line) and the media thickness reflecting the intracoronary pressure (red line).

(F) Spectral curves at the selected time points. Spectral centroid λ_c in (E and F) is extracted from the nonframe-averaged spectral centroid shift images.

backscattering property. The lack of specificity for tissue components and functional states has been the main shortcoming of optical reflectance techniques. The geometry-dependent spectroscopic contrasts may enable us to specifically distinguish nano-cylinders from spherical scatterers or even extract functional information of biological systems. First of all, this geometry-dependent spectroscopic contrast may be particularly useful for imaging applications where the sub-diffraction-limit structures and processes cannot be optimally visualized and differentiated. Analysis of ciliary beat pattern has been proposed as a powerful method to diagnose primary ciliary dyskinesia (PCD) (Chilvers and O'callaghan, 2000; Chilvers et al., 2003), since the current ciliary beat frequency method and ultrastructural analysis may not be accurate (Buchdahl et al., 1988; Rossman and Newhouse, 1988; Santamaria et al., 1999). The most common motility defect of PCD is the inability to bend along the axoneme (Chilvers and O'callaghan, 2000; Chilvers et al., 2003), which may be identified as the lack of the signature spectral centroid shift toward the long wavelengths from the bending cilia in the recovery stroke.

In addition, it is important to understand the effects of the degree of alignment on the spectroscopic contrast. In our simulations, the model collagen fibrils are well aligned and tightly packed and diffract light at roughly the same spacing (Table S2). If the orientation of individual fibrils was random, these mis-aligned nano-cylinders exhibited no significant collective spectral centroid shifts (Figure 3B), which is consistent with the experimental observations in the papillary dermis: loosely arranged collagen fibrils and elastic fibers with random orientations appeared to be neutral and heterogeneous in the spectral centroid shift (Figures S4D–S4F). Even under the aligned condition, the spectral centroid shift of nanoscale fibrous structures is dependent on their spacing (Figure S6). When we increased the interfibrillar spacing from 1D to 1.05D, the peak and valley shifted monotonically; further increase in the interfibrillar spacing may result in an inversion of spectral centroid shift.

There have been theoretical techniques for characterizing the light scattering of the biological tissue that were treated as either a continuously random medium (Rogers et al., 2009; Schmitt and Kumar, 1996; Sheppard, 2007; Xu and Alfano, 2005) or medium having spatial quasi-ordered distribution of scatterers (Hart

and Farrell, 1969; Zimm, 1948). In the former treatment, the biological tissue is assumed as a homogeneous and isotropic medium, and a continuous refractive index (RI) fluctuation is dependent on the fractal dimension D_f. Based on the previous measurements, the D_f values ranged from 2.6 to 3.1 for different types of soft tissues (Schmitt and Kumar, 1996; Yi and Backman, 2012). Since the backscattering coefficient $\mu_b \propto \lambda^{D_f-4}$ where a smaller D_f corresponds to a smaller length scale RI variation (Yi et al., 2013), backscattered spectra contributed by these nano-structures in the Rayleigh regime must show a blue-shift phenomenon. Therefore, this treatment may not be applied to packed nano-cylinders. The latter treated the spatial inhomogeneity of fibrils as a quasi-crystalline arrangement, described by the radial distribution function. Taking into account the interference effects, the transparency of the cornea (Hart and Farrell, 1969) and the transmission property of the sclera (Tuchin et al., 1997) were well characterized. The latter treatment is more suitable for our study because the cylindrical center positions could be correlated over distances comparable with the wavelength so that the interference between the scattered fields should be accounted for. The radial distribution function is defined by the ratio of a local density of the scatterers' centers within a circular ring ranges from x to $x + \Delta x$, to the mean density of the scatterers' centers in that ring. The analytic form of the backscattering coefficient in the far field is given by:

$$\mu_b = \frac{d_c}{\pi r^2}\int_{\pi-\theta_{\max}}^{\pi+\theta_{\max}} \sigma_0(\theta)\left\{1 + 2\pi\rho\int_0^L x dx[g(x)-1]J_0\left[2\bar{k}x\sin\left(\frac{\theta}{2}\right)\right]\right\}d\theta \qquad \text{(Equation 1)}$$

where d_c is the cross-sectional packing fraction of nano-cylinders, r is the radius of nano-cylinders, $\sin\theta_{\max} = N.A.$ is the numerical aperture of the objective, σ_0 is the backscattering cross section of a single nano-cylinder, $\bar{k} = 2\pi\bar{n}/\lambda$, λ is the wavelength in the vacuum, $m = n_c/n_m$ is the ratio of RI of the nano-cylinders n_c to that of the surrounding medium n_m, average RI $\bar{n} = d_c n_c + (1 - d_c)n_m = n_m[d_c(m-1)]$, L should be larger than the correlation distance L_R above which the $g(x)$ is essentially unity, and J_0 is the zero-order Bessel function of the first kind. Derivation of Equation 1 and variable analysis are provided in detail in the Transparent Methods. Although $g(x)$ can be measured in simulations or electron micrographs, for the sake of analysis, we followed the approach (Yuste and Santos, 1993) that $g(x)$ is generated by the packing fraction d_c. Figure S7A shows the undulatory property of $g(x)$ at $d_c = 0.3$, $d_c = 0.5$, and $d_c = 0.7$. A larger d_c value corresponds to a longer correlation distance L_R of nano-cylinders' centers. The first peak in $g(x)$ indicates the diameter of nano-cylinders as they cannot overlap. From the Figures S7B–S7D, in terms of radius from 10 to 50 nm, the backscattered intensity always decays with λ when the correlation distance L_R is short (i.e., d_c is in small value). However, some of cancellation or upward slopes in the spectral curves appear when d_c is larger, indicating the possibility of long-wavelength shifts caused by the constructive and destructive interference.

In our FDTD simulations, we were not able to establish theoretical models of all the above-mentioned complex biological systems owing to the lack of reliable data on the optical properties and spatial arrangements of nanoscale cylindrical structures. Even for the simplest systems such as motile cilia and lamina cribrosa/sclera, assumptions were made and much simplified models with estimated parameters were used. For example, as the refractive index of motile cilia and the surrounding liquid is unknown, we used estimated data reported in the previous literature (Schmitt and Kumar, 1998; Welch et al., 2005). Therefore, one should be careful in interpreting the data because the spectroscopic metric is cumulative as the random medium will also alter the spectrum, and interpretation of spectral data in anatomically complex scenarios are prone to the artifacts caused by the cumulative influence of random medium in the light path. These shortcomings of the theoretical approach are primarily compensated by careful selection of simple biological models and SOCT-based experimental verifications. Nevertheless, we tested numerically whether variation in the refractive index of cilia might alter the results. The centroid of the spectrum from a representative motile cilia model shifted 9.3 nm toward the long wavelengths caused by a difference in the refractive index from 1.40 to 1.60 (Figure S8), which indicates that the refractive index of the cilia may not be a critical factor for the spectroscopic contrast.

Unlike previous observations in mouse models that the spectral centroid of the normal dermis shifted to the short (Maher et al., 2014; Zhao et al., 2015), our results showed that the spectral centroid of mouse dermis shifts more toward the long wavelengths than the short. We postulated that it might be due to the differences in axial resolution, spectral data presentation and interpretation, and compositions of the dermis. First of all, Maher and Zhao's works reported the collective spectral change of the whole skin, where contributions from individual skin layers or components were not differentiated or interpreted in the spectral data (Zhao et al., 2015). Actually, with an axial resolution of 60 μm, collagen fibers cannot be differentiated

from other tissue components. In contrast, our work aims to specifically investigate the spectral change of collagen fibers, which is the reason why we set the spatial resolution to ~4 μm in tissue to differentiate the spectroscopic signals of different tissue components and collagen fibers of different orientation/packing state. Second, the compositions of the dermis are quite different between the previous works and our work. Maher and Zhao's works chose dorsal skin that contained a lot of subdermal adipose and muscle tissues. With an axial resolution of 60 μm, the spectroscopic signals from individual collagen fibers might have been averaged with those from other scatterers in the focal volume. Anyway, we can still find some remnant signals of long-wavelength-shifted spectral centroid in the spectroscopic image (Maher et al., 2014). In contrast, in our study we chose ear skin, which does not contain as many adipose and muscle tissues. Third, in our experiment the ear dermis was stretched horizontally by its cartilages, which served our purpose to have more regularly arranged collagen fibrils (Figure S9). We have no way to know if the dorsal skin was stretched or not during the experiments of the previous reports, but from the curvy tissue surfaces in OCT images (Maher et al., 2014) we can tell that they were not stretched as much as the ear dermis in our experiments (Figure 4).

In conclusion, we uncovered the geometry dependency of the reflectance spectroscopic signals of nanoscale scatterers and established a theoretical and experimental approach to understand and characterize the spectroscopic behaviors of mammalian deep tissue models containing nanoscale cylindrical structures. The signature spectral centroid shift from bending cilia may provide a complementary method to noninvasively detect the motility defect of cilia, thereby benefiting the diagnosis PCD. The correlation between the spectral centroid shift and stress may open up a new avenue to qualitatively or semi-quantitatively monitor the localized pressure of body fluid, in particular, the intravascular and intraocular pressure, for the study and diagnosis of vascular and ocular diseases.

Limitations of the Study

As mentioned in the discussion, approximations were made in the FDTD simulation and the theoretical derivation. We considered only the transverse orientation (perpendicular to the input beam) of nano-cylinders based on the fact that the backscattered intensity of the transversely oriented nano-cylinders was significantly greater than that of any other orientation (data not shown). The crimped or helical form of fibrils was approximated by parallel nano-cylinders in this study because the wavelength of a cylindrical helix (10–100 μm) is much larger than the resolution element (Freed and Doehring, 2005). Meanwhile, the absorption property of nanostructures should be taken into account in the absorption-dominant wavelength regions (Robles et al., 2011).

METHODS

All methods can be found in the accompanying Transparent Methods supplemental file.

SUPPLEMENTAL INFORMATION

Supplemental Information can be found online at https://doi.org/10.1016/j.isci.2019.08.046.

ACKNOWLEDGMENTS

This research was supported by Agency for Science, Technology and Research (A*STAR) under its Industrial Alignment Fund (Pre-positioning) (H17/01/a0/008), National Natural Science Foundation of China (Grant No. 61540042 & No. 61705184), Natural Science Basic Research Plan in Shaanxi Province of China (Grant No. 2018JQ6014), Ministry of Education - Singapore (MOE2013-T2-2-107 & RG 83/18 & RG 131/15), National Research Foundation Singapore (NRF-CRP13-2014-05), National Medical Research Council Singapore (NMRC/CBRG/0036/2013), NTU-Northwestern Institute for Nanomedicine, and the Fundamental Research Funds for the Central Universities (Grant No. G2018KY0308).

AUTHOR CONTRIBUTIONS

X.G., S.M.R., G.J.T., and L.L. conceived and designed the research. X.G., H.T., X.W., S.C., and L.L. conducted experiments. X.G. conducted theoretical analysis and numerical simulation; X.L., X.W., and H.T. contributed to the SOCT algorithm; all authors contributed to the imaging studies and data analysis. X.G. and L.L. co-wrote the manuscripts. S.M.R., G.J.T., and L.L. supervised the overall project. All authors read and edited the manuscript.

DECLARATION OF INTERESTS

The authors declare no competing interests.

Received: March 9, 2019
Revised: July 10, 2019
Accepted: August 22, 2019
Published: September 27, 2019

REFERENCES

Abdullahi, A., Amini-Nik, S., and Jeschke, M. (2014). Animal models in burn research. Cell. Mol. Life Sci. *71*, 3241–3255.

Azarin, S.M., Yi, J., Gower, R.M., Aguado, B.A., Sullivan, M.E., Goodman, A.G., Jiang, E.J., Rao, S.S., Ren, Y., and Tucker, S.L. (2015). In vivo capture and label-free detection of early metastatic cells. Nat. Commun. *6*, 8094.

Barrick, J., Doblas, A., Gardner, M.R., Sears, P.R., Ostrowski, L.E., and Oldenburg, A.L. (2016). High-speed and high-sensitivity parallel spectral-domain optical coherence tomography using a supercontinuum light source. Opt. Lett. *41*, 5620–5623.

Buchdahl, R., Reiser, J., Ingram, D., Rutman, A., Cole, P., and Warner, J. (1988). Ciliary abnormalities in respiratory disease. Arch. Dis. Child. *63*, 238–243.

Chilvers, M.A., and O'callaghan, C. (2000). Analysis of ciliary beat pattern and beat frequency using digital high speed imaging: comparison with the photomultiplier and photodiode methods. Thorax *55*, 314–317.

Chilvers, M.A., Rutman, A., and O'callaghan, C. (2003). Ciliary beat pattern is associated with specific ultrastructural defects in primary ciliary dyskinesia. J. Allergy Clin. Immunol. Pract. *112*, 518–524.

Cuthill, I.C., Allen, W.L., Arbuckle, K., Caspers, B., Chaplin, G., Hauber, M.E., Hill, G.E., Jablonski, N.G., Jiggins, C.D., and Kelber, A. (2017). The biology of color. Science *357*, eaan0221.

Dingemans, K.P., Teeling, P., Lagendijk, J.H., and Becker, A.E. (2000). Extracellular matrix of the human aortic media: an ultrastructural histochemical and immunohistochemical study of the adult aortic media. Anat. Rec. *258*, 1–14.

Freed, A.D., and Doehring, T.C. (2005). Elastic model for crimped collagen fibrils. J. Biomech. Eng. *127*, 587–593.

Fujimoto, J.G. (2003). Optical coherence tomography for ultrahigh resolution in vivo imaging. Nat. Biotechnol. *21*, 1361.

Hart, R.W., and Farrell, R.A. (1969). Light scattering in the cornea. JOSA *59*, 766–774.

Hooke, R. (1665). Micrographia: Or Some Physiological Descriptions of Minute Bodies Made by Magnifying Glasses, with Observations and Inquiries Thereupon (John Martyn and James Allestry).

Huang, D., Swanson, E.A., Lin, C.P., Schuman, J.S., Stinson, W.G., Chang, W., Hee, M.R., Flotte, T., Gregory, K., and Puliafito, C.A. (1991). Optical coherence tomography. Science *254*, 1178–1181.

Kim, J.S., Pradhan, P., Backman, V., and Szleifer, I. (2011). The influence of chromosome density variations on the increase in nuclear disorder strength in carcinogenesis. Phys. Biol. *8*, 015004.

Komai, Y., and Ushiki, T. (1991). The three-dimensional organization of collagen fibrils in the human cornea and sclera. Investig. Ophthalmol. Vis. Sci. *32*, 2244–2258.

Leitgeb, R., Wojtkowski, M., Kowalczyk, A., Hitzenberger, C., Sticker, M., and Fercher, A. (2000). Spectral measurement of absorption by spectroscopic frequency-domain optical coherence tomography. Opt. Lett. *25*, 820–822.

Liu, L., Chu, K.K., Houser, G.H., Diephuis, B.J., Li, Y., Wilsterman, E.J., Shastry, S., Dierksen, G., Birket, S.E., and Mazur, M. (2013). Method for quantitative study of airway functional microanatomy using micro-optical coherence tomography. PLoS One *8*, e54473.

Liu, L., Gardecki, J.A., Nadkarni, S.K., Toussaint, J.D., Yagi, Y., Bouma, B.E., and Tearney, G.J. (2011). Imaging the subcellular structure of human coronary atherosclerosis using micro–optical coherence tomography. Nat. Med. *17*, 1010.

Maher, J.R., Jaedicke, V., Medina, M., Levinson, H., Selim, M.A., Brown, W.J., and Wax, A. (2014). In vivo analysis of burns in a mouse model using spectroscopic optical coherence tomography. Opt. Lett. *39*, 5594–5597.

Morgner, U., Drexler, W., Kärtner, F., Li, X., Pitris, C., Ippen, E., and Fujimoto, J. (2000). Spectroscopic optical coherence tomography. Opt. Lett. *25*, 111–113.

Moyroud, E., Wenzel, T., Middleton, R., Rudall, P.J., Banks, H., Reed, A., Mellers, G., Killoran, P., Westwood, M.M., and Steiner, U. (2017). Disorder in convergent floral nanostructures enhances signalling to bees. Nature *550*, 469.

Newton, I. (1704). Opticks, or, a Treatise of the Reflections, Refractions, Inflections & Colours of Light (Reprinted by Dover Publications).

Oldenburg, A.L., Chhetri, R.K., Hill, D.B., and Button, B. (2012). Monitoring airway mucus flow and ciliary activity with optical coherence tomography. Biomed. Opt. Express *3*, 1978–1992.

Oldenburg, A.L., Xu, C., and Boppart, S.A. (2007). Spectroscopic optical coherence tomography and microscopy. IEEE J. Sel. Top. Quant. Electron. *13*, 1629–1640.

Quigley, H.A., Dorman-Pease, M.E., and Brown, A.E. (1991). Quantitative study of collagen and elastin of the optic nerve head and sclera in human and experimental monkey glaucoma. Curr. Eye Res. *10*, 877–888.

Robles, F.E., and Wax, A. (2010). Measuring morphological features using light-scattering spectroscopy and Fourier-domain low-coherence interferometry. Opt. Lett. *35*, 360–362.

Robles, F.E., Wilson, C., Grant, G., and Wax, A. (2011). Molecular imaging true-colour spectroscopic optical coherence tomography. Nat. Photonics *5*, 744–747.

Robles, F.E., Zhu, Y., Lee, J., Sharma, S., and Wax, A. (2010). Detection of early colorectal cancer development in the azoxymethane rat carcinogenesis model with Fourier domain low coherence interferometry. Biomed. Opt. Express *1*, 736–745.

Rogers, J.D., Çapoğlu, İ.R., and Backman, V. (2009). Nonscalar elastic light scattering from continuous random media in the Born approximation. Opt. Lett. *34*, 1891–1893.

Rossman, C.M., and Newhouse, M.T. (1988). Primary ciliary dyskinesia: evaluation and management. Pediatr. Pulmonol. *5*, 36–50.

Sanderson, M., and Sleigh, M. (1981). Ciliary activity of cultured rabbit tracheal epithelium: beat pattern and metachrony. J. Cell Sci. *47*, 331–347.

Santamaria, F., De Santi, M., Grillo, G., Sarnelli, P., Caterino, M., and Greco, L. (1999). Ciliary motility at light microscopy: a screening technique for ciliary defects? Acta Paediatr. *88*, 853–857.

Schmitt, J., and Kumar, G. (1996). Turbulent nature of refractive-index variations in biological tissue. Opt. Lett. *21*, 1310–1312.

Schmitt, J.M., and Kumar, G. (1998). Optical scattering properties of soft tissue: a discrete particle model. Appl. Opt. *37*, 2788–2797.

Sheppard, C.J. (2007). Fractal model of light scattering in biological tissue and cells. Opt. Lett. *32*, 142–144.

Tearney, G.J., Brezinski, M.E., Bouma, B.E., Boppart, S.A., Pitris, C., Southern, J.F., and Fujimoto, J.G. (1997). In vivo endoscopic optical biopsy with optical coherence tomography. Science *276*, 2037–2039.

Teyssier, J., Saenko, S.V., Van Der Marel, D., and Milinkovitch, M.C. (2015). Photonic crystals cause active colour change in chameleons. Nat. Commun. *6*, 6368.

Tseng, S.H., Taflove, A., Maitland, D., and Backman, V. (2006). Pseudospectral time domain simulations of multiple light scattering in three-dimensional macroscopic random media. Radio Sci. *41*, 1–5.

Tuchin, V.V., Maksimova, I.L., Zimnyakov, D.A., Kon, I.L., Mavlyutov, A.H., and Mishin, A.A. (1997). Light propagation in tissues with controlled optical properties. J. Biomed. Opt. *2*, 401–418.

Uttam, S., Pham, H.V., LaFace, J., Leibowitz, B., Yu, J., Brand, R.E., Hartman, D.J., and Liu, Y. (2015). Early prediction of cancer progression by depth-resolved nanoscale mapping of nuclear architecture from unstained tissue specimens. Cancer Res. *75*, 4718–4727.

Vignolini, S., Rudall, P.J., Rowland, A.V., Reed, A., Moyroud, E., Faden, R.B., Baumberg, J.J., Glover, B.J., and Steiner, U. (2012). Pointillist structural color in Pollia fruit. Proc. Natl. Acad. Sci. U S A *109*, 15712–15715.

Vukusic, P., and Sambles, J.R. (2003). Photonic structures in biology. Nature *424*, 852–855.

Wang, P., Bista, R.K., Khalbuss, W.E., Qiu, W., Uttam, S., Staton, K.D., Zhang, L., Brentnall, T.A., Brand, R.E., and Liu, Y. (2010). Nanoscale nuclear architecture for cancer diagnosis beyond pathology via spatial-domain low-coherence quantitative phase microscopy. J. Biomed. Opt. *15*, 066028.

Wax, A., Terry, N.G., Dellon, E.S., and Shaheen, N.J. (2011). Angle-resolved low coherence interferometry for detection of dysplasia in Barrett's esophagus. Gastroenterology *141*, 443–447, 447.e1–e2.

Welch, V., Vigneron, J., and Parker, A. (2005). The cause of colouration in the ctenophore *Beroe cucumis*. Curr. Biol. *15*, R985–R986.

Wiersma, D.S. (2013). Disordered photonics. Nat. Photonics *7*, 188–196.

Xu, C., Carney, P.S., and Boppart, S.A. (2005). Wavelength-dependent scattering in spectroscopic optical coherence tomography. Opt. Express *13*, 5450–5462.

Xu, C., Vinegoni, C., Ralston, T.S., Luo, W., Tan, W., and Boppart, S.A. (2006). Spectroscopic spectral-domain optical coherence microscopy. Opt. Lett. *31*, 1079–1081.

Xu, M., and Alfano, R.R. (2005). Fractal mechanisms of light scattering in biological tissue and cells. Opt. Lett. *30*, 3051–3053.

Yang, W., Sherman, V.R., Gludovatz, B., Schaible, E., Stewart, P., Ritchie, R.O., and Meyers, M.A. (2015). On the tear resistance of skin. Nat. Commun. *6*, 6649.

Yelin, D., Rizvi, I., White, W., Motz, J., Hasan, T., Bouma, B., and Tearney, G. (2006). Three-dimensional miniature endoscopy. Nature *443*, 765.

Yi, J., and Backman, V. (2012). Imaging a full set of optical scattering properties of biological tissue by inverse spectroscopic optical coherence tomography. Opt. Lett. *37*, 4443–4445.

Yi, J., Radosevich, A.J., Rogers, J.D., Norris, S.C., Çapoğlu, İ.R., Taflove, A., and Backman, V. (2013). Can OCT be sensitive to nanoscale structural alterations in biological tissue? Opt. Express *21*, 9043–9059.

Yun, S.H., Tearney, G.J., Vakoc, B.J., Shishkov, M., Oh, W.Y., Desjardins, A.E., Suter, M.J., Chan, R.C., Evans, J.A., and Jang, I.-K. (2006). Comprehensive volumetric optical microscopy in vivo. Nat. Med. *12*, 1429.

Yuste, S.B., and Santos, A. (1993). Radial distribution function for sticky hard-core fluids. J. Stat. Phys. *72*, 703–720.

Zhao, Y., Maher, J.R., Kim, J., Selim, M.A., Levinson, H., and Wax, A. (2015). Evaluation of burn severity in vivo in a mouse model using spectroscopic optical coherence tomography. Biomed. Opt. Express *6*, 3339–3345.

Zimm, B.H. (1948). The scattering of light and the radial distribution function of high polymer solutions. J. Chem. Phys. *16*, 1093–1099.

ISCI, Volume *19*

Supplemental Information

Geometry-Dependent Spectroscopic Contrast in Deep Tissues

Xin Ge, Hongying Tang, Xianghong Wang, Xinyu Liu, Si Chen, Nanshuo Wang, Guangming Ni, Xiaojun Yu, Shufen Chen, Haitao Liang, En Bo, Lulu Wang, Cilwyn Shalitha Braganza, Chenjie Xu, Steven M. Rowe, Guillermo J. Tearney, and Linbo Liu

Supplemental Figures

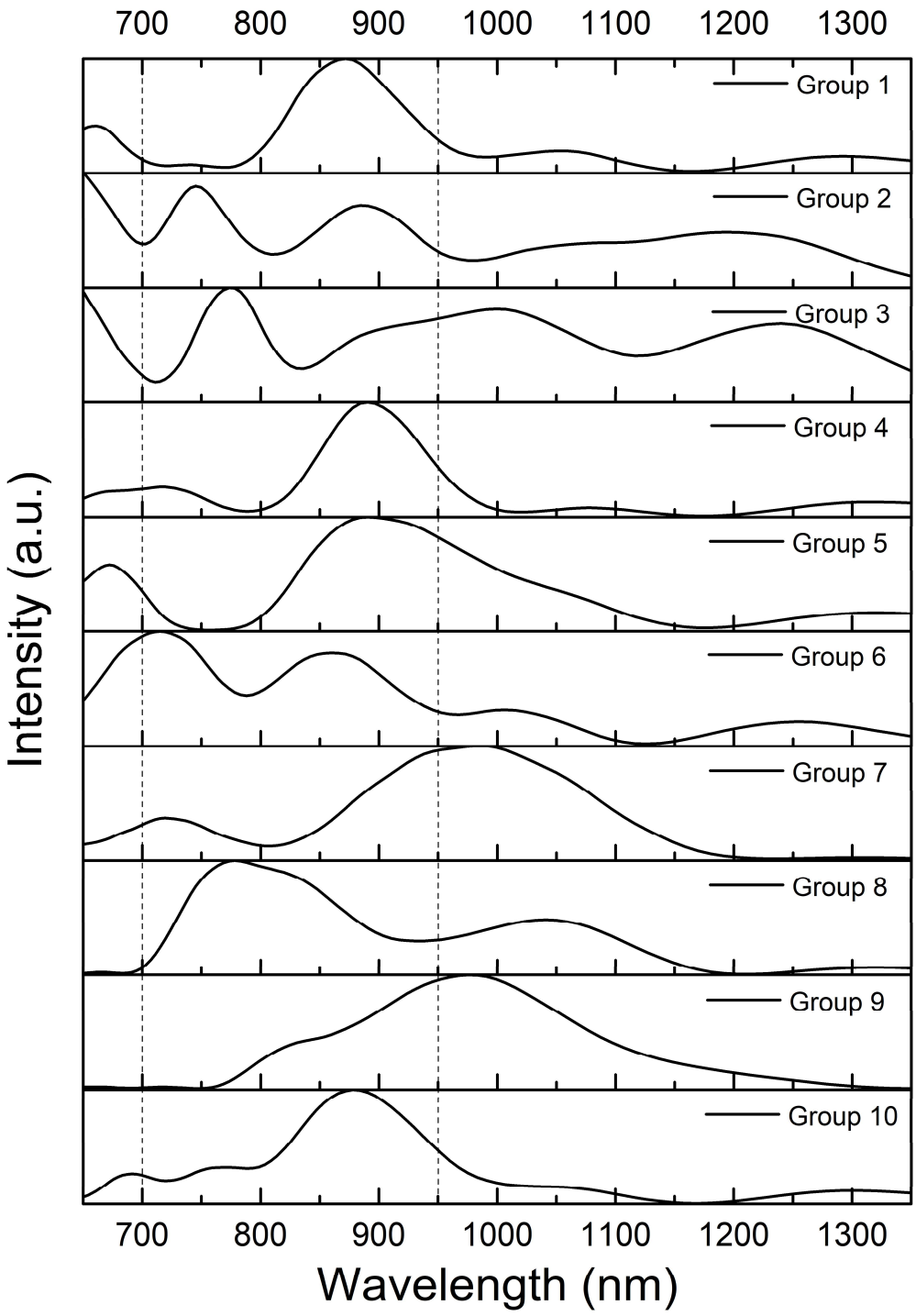

Figure S1. Normalized backscattered spectra from 10 groups of packed nano-cylinders simulating motile cilia in the entire near-infrared region (650-1350 nm), related to Figure 1B. The spectral window of 700-950 nm was between two dashed lines.

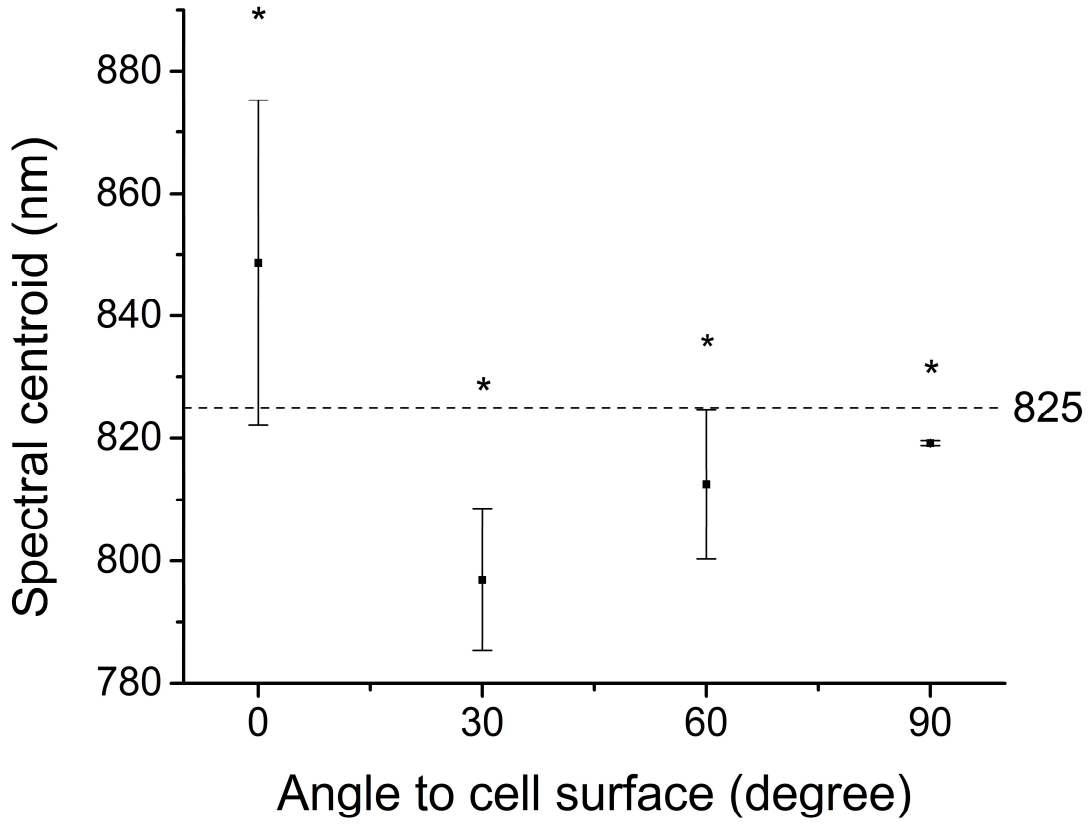

Figure S2. Angle-dependent spectral centroid shift statistically analyzed in the cilia model, related to Figure 1B. The mean spectral centroid (solid rectangle) of 10 groups of packed nano-cylinders with axes of the cylinders at tiled 0°, 30°, 60° and 90° relative to the apical cell surface. Error bar = SD. * p<0.05 by Student's one sample t-test compared with the test mean value λ=825 nm from 700-950 nm. The p-values were $7.4e^{-3}$ (right-tailed), $3.9e^{-4}$ (left-tailed), $5.8e^{-3}$ (left-tailed), $3.4e^{-11}$ (left-tailed), in order.

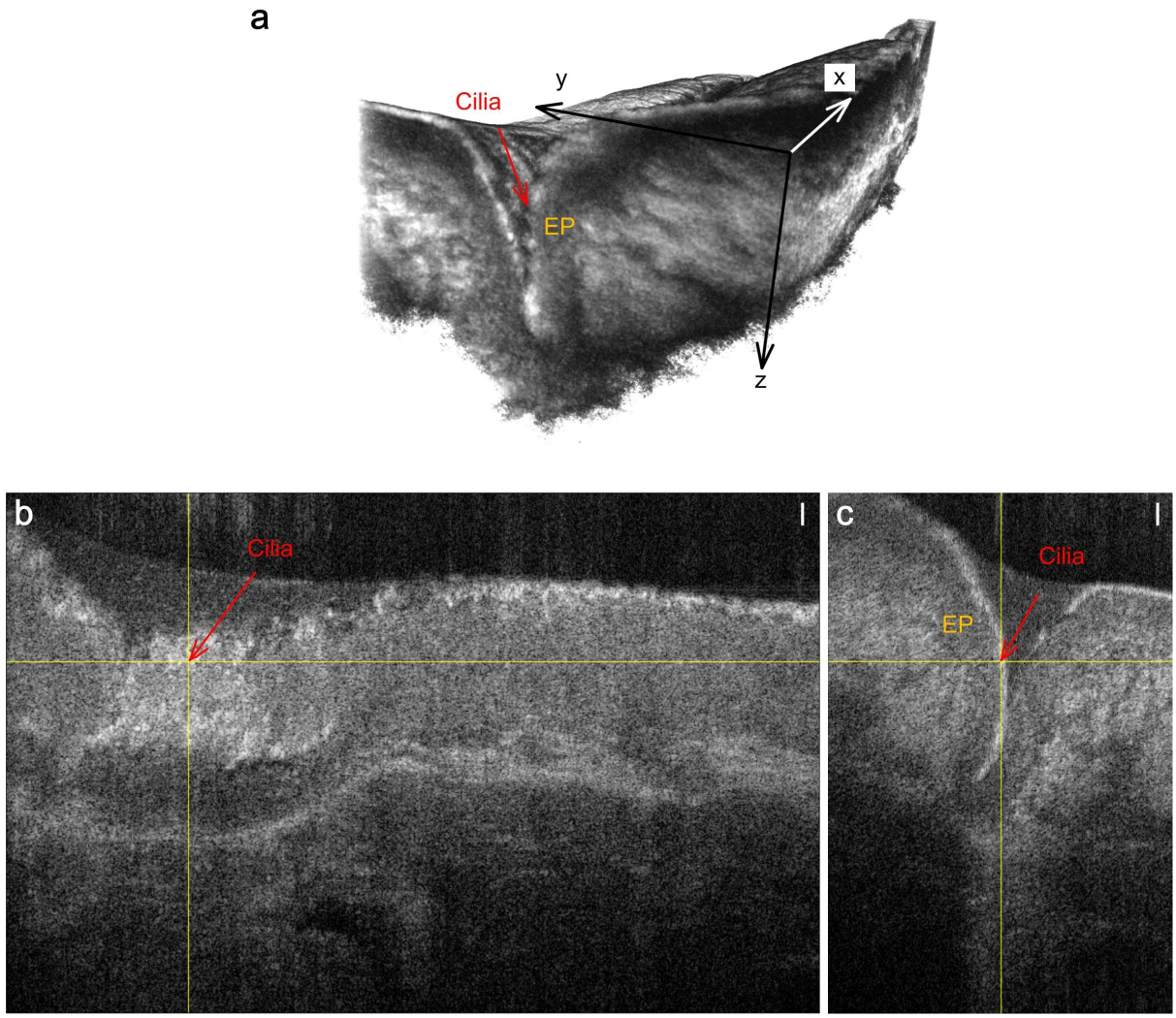

Figure S3. 3D and orthographic views of the sheep respiratory epithelium (EP), related to Figure 2D. (a) 3D view depicting the epithelium folding. (b) the x-z view (**Figure 2D)** was parallel to the epithelial surface, which can be seen clearly in the orthographically projected y-z view in (c). Scale bars: 10 μm.

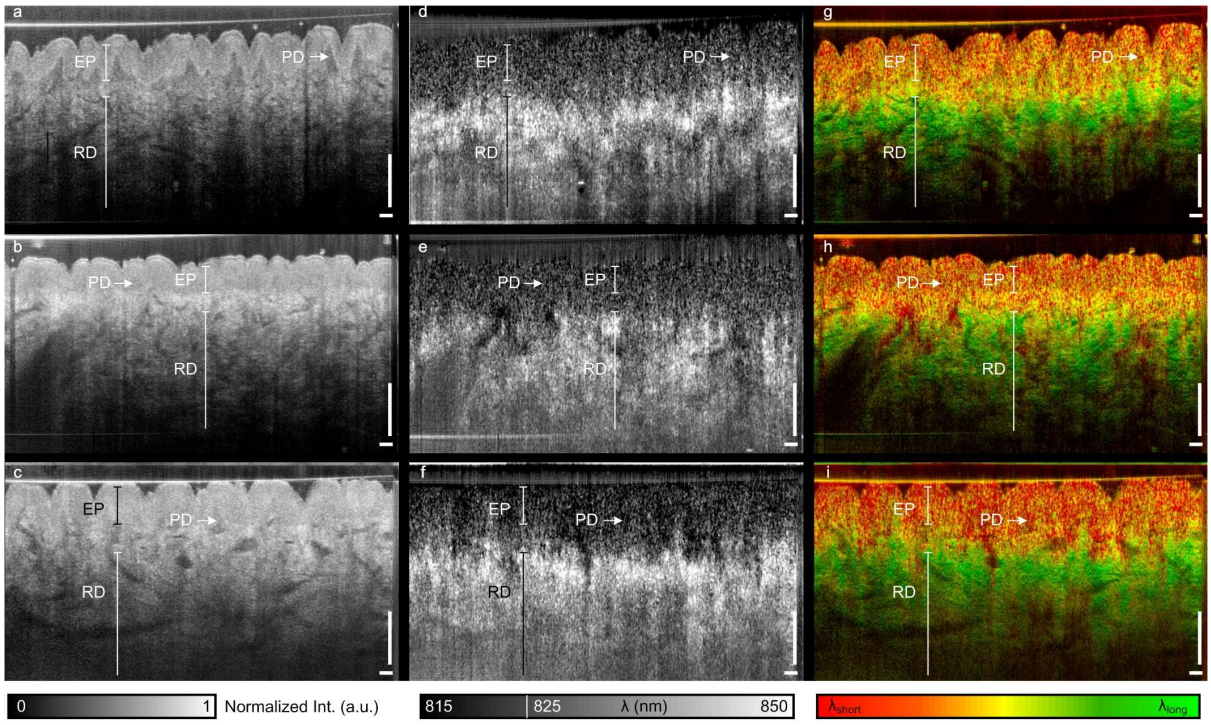

Figure S4. Cross-sectional images of human skin of different phenotypes *in vivo*, related to Figure 3. Representative intensity image, spectral centroid shift image, and HSV-mapped SOCT image of human skin *in vivo* from (**a, d, g**) dark-skinned volunteers, (**b, e, h**) light-skinned volunteers and (**c, f, i**) volunteers with medium skin pigmentation. EP: epidermis, PD: papillary dermis and RD: reticular dermis. Scale bars: 100 μm.

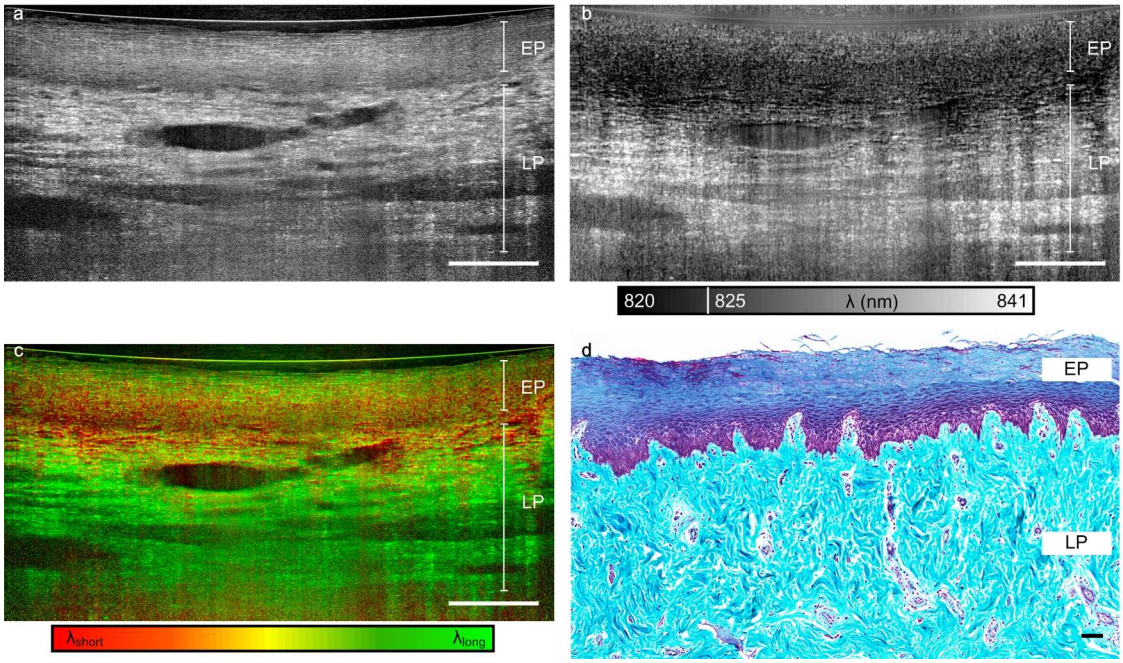

Figure S5. Cross-sectional image of the swine oesophagus *in vivo*, related to Figure 3. Representative (**a**) OCT intensity image, (**b**) Spectral centroid shift image, (**c**) HSV-mapped SOCT image and (**d**) Corresponding Masson's trichrome stained histology image. EP: epithelium; LP: lamina propria. Scale bars: 100 μm.

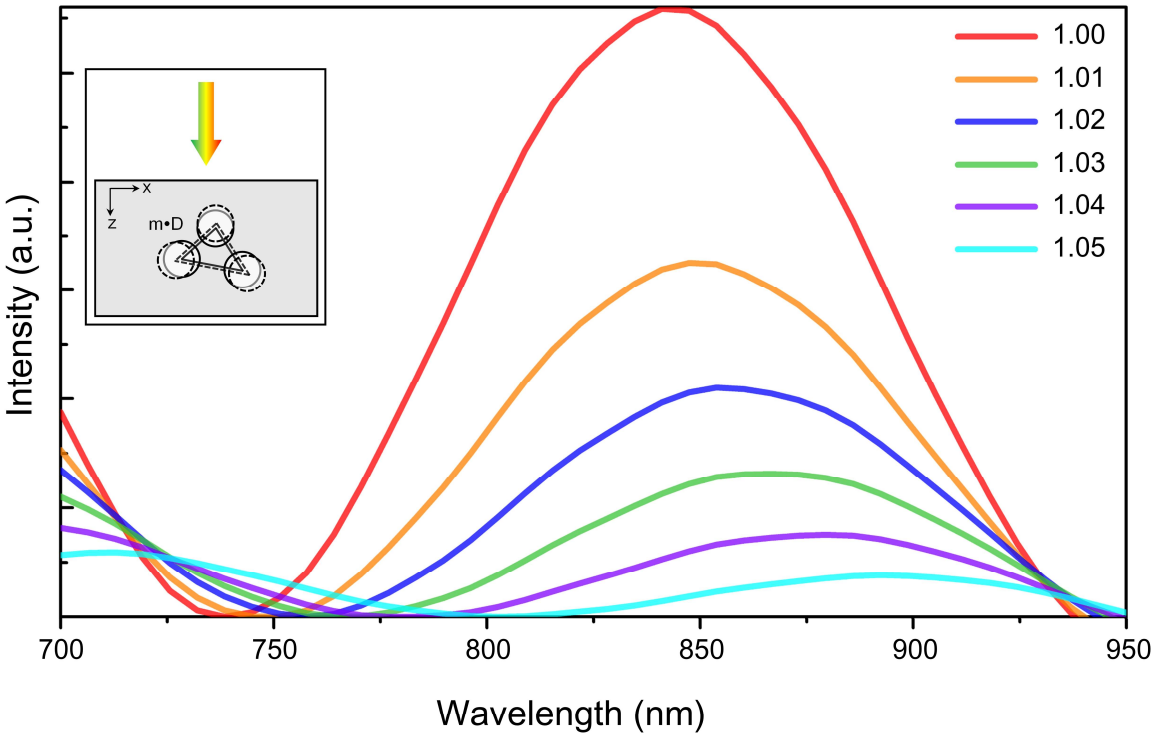

Figure S6. FDTD simulation on the effect of changing interfibrillar spacing m·D between well-aligned collagen fibrils, related to Figure 3A. m is the magnification ratio. Backscattered spectra were normalized by the minimum value of each curve. The curve valley shifts 86 nm towards long wavelengths upon a change in the magnification ratio from 1.00 to 1.05.

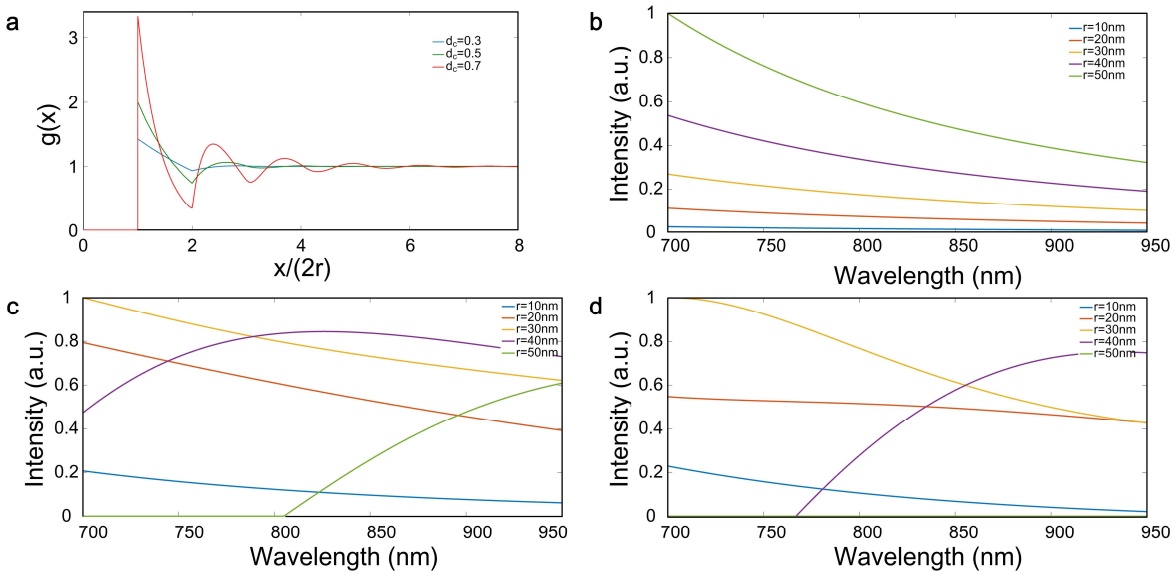

Figure S7. (a) Radial distribution function g(x) for non-sticky hard cylinders at several values of the packing fraction d_c. The largest peak of each curve corresponds to the smallest interfibrillar spacing, which is equal to the diameter. (b-c) Normalized spectra for the packing faction d_c=0.3, d_c=0.5 and d_c=0.7, the radius of cylinder r is varied from 10 nm to 50 nm. This is related to **Figure 3A**.

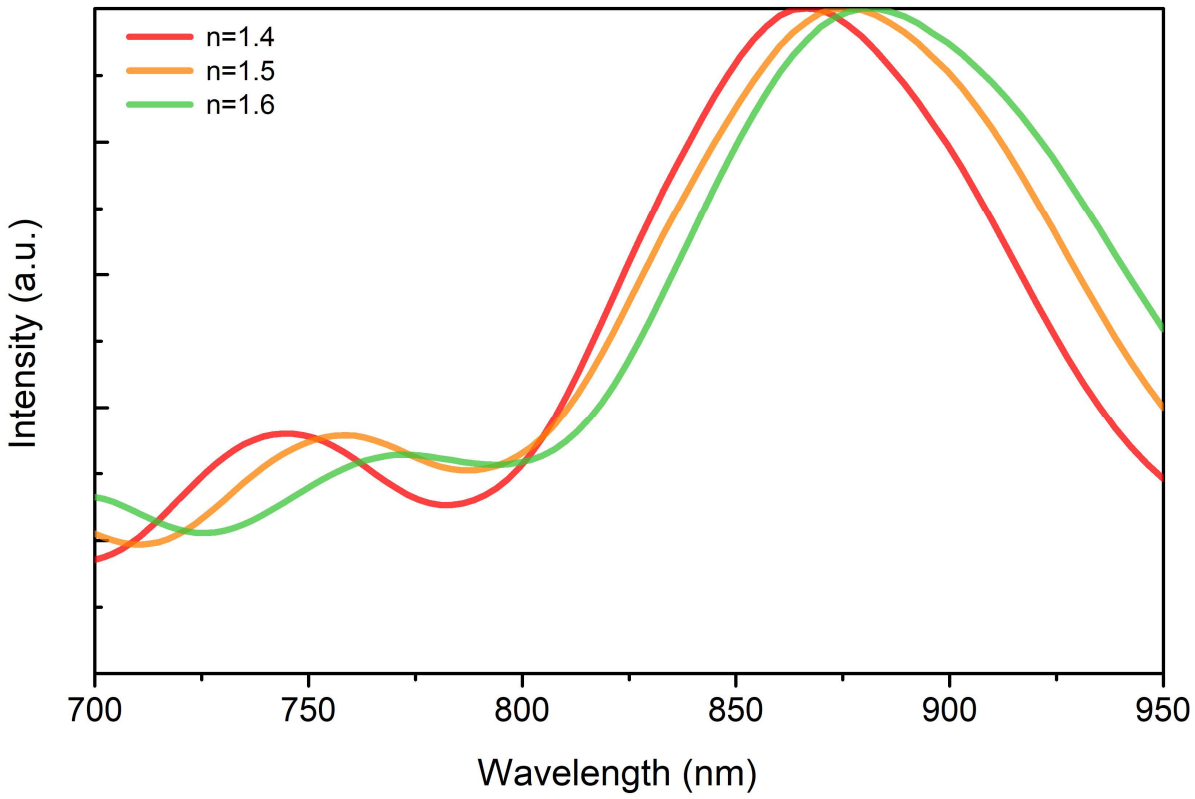

Figure S8. Effect of refractive index variations on the spectroscopic contrast of motile cilia, related to Figure 1B. Backscattered spectra from a representative model of motile cilia with different refractive indices (n). Each spectrum was normalized to its peak. Respective centroid c is 846.4 nm, 851.4 nm and 855.7 nm.

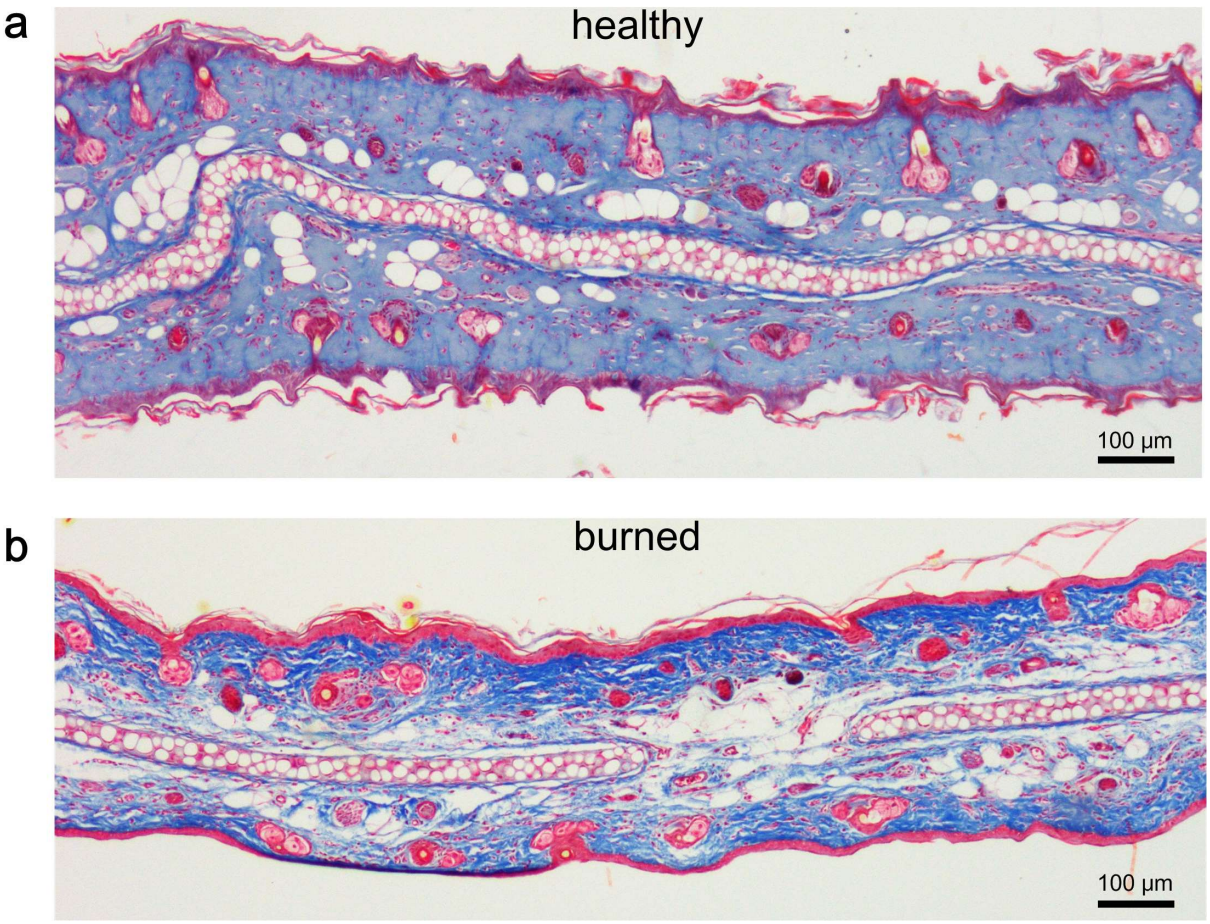

Figure S9. Masson's trichrome stained histology images of healthy (a) and burned (b) mouse ear, related to Figure 4.

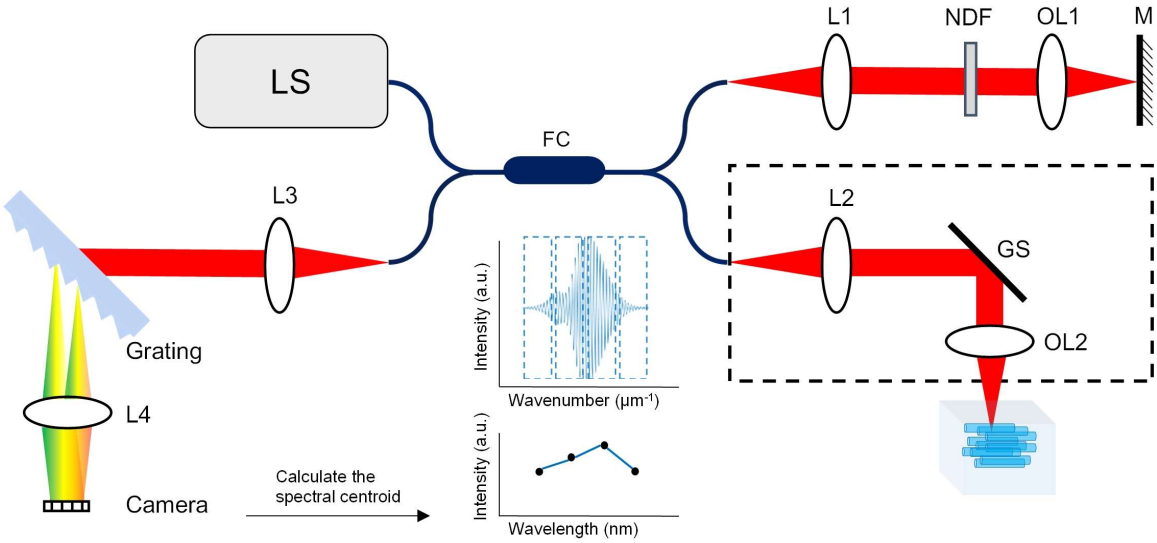

Figure S10. Schematic of the SOCT system and short-frequency Fourier transform (SFFT) processing, related to Figure 2B, 2E, 3D, 4B, 4E, 5C and 5D. LS: Light source, FC: 50/50 fiber coupler, L1-4: optical lens, OL1-2: objective lens, M: mirror, GS: galvo scanner, NDF: neutral density filter and handheld probe (black dashed box).

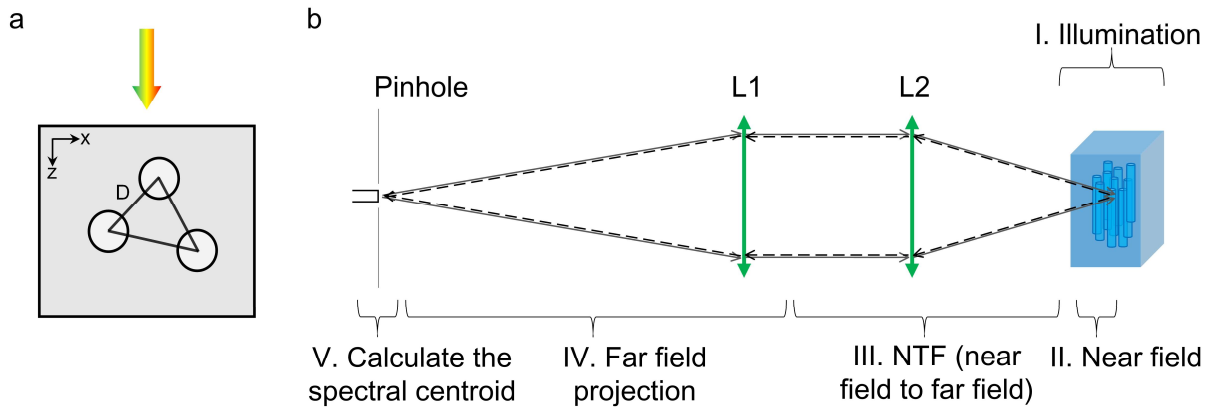

Figure S11. Schematic of scatterers generation strategy and light propagation through the OCT sample arm, related to Figure 1B, 1C, 3A and 3B. (**a**) Approach to the placement of non-overlapping scatterers with a spacing distance D at random positions. (**b**) Computational imaging in the sample arm of SOCT.

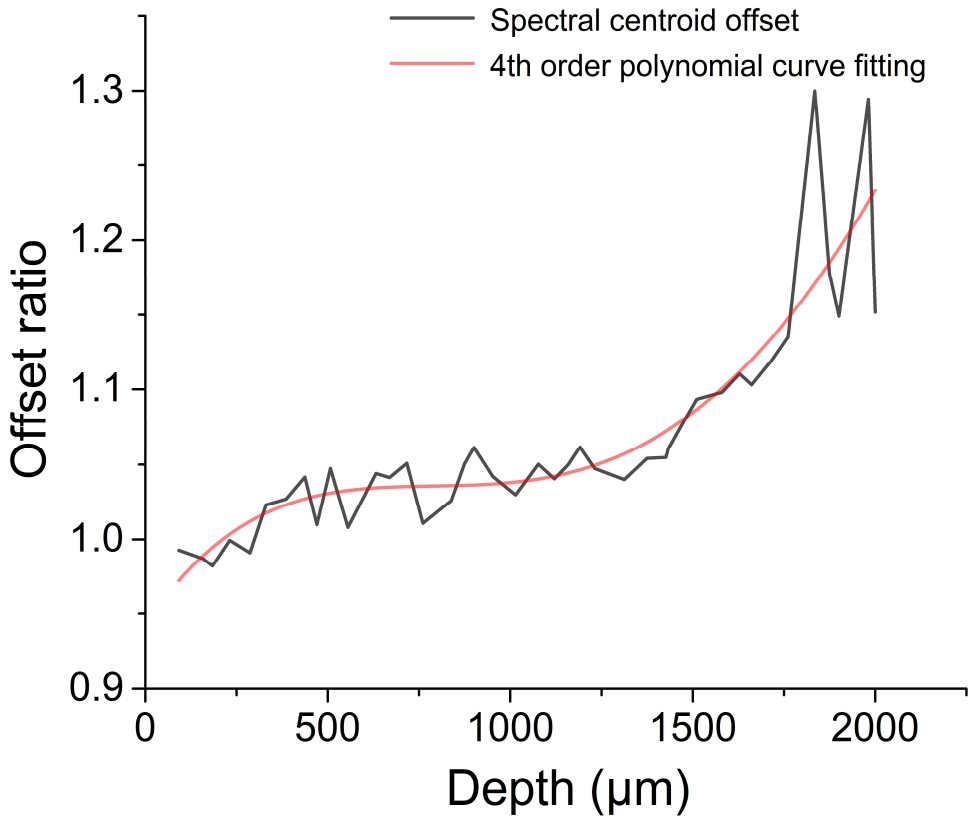

Figure S12. Depth-dependent spectral centroid offset due to wavenumber-space nonlinearity, related to Figure 2B, 2E, 3D, 4B, 4E, 5C and 5D. The black curve indicates the measured spectral centroid with a perfect reflector at different imaging depths. We used the 4th order polynomial fitting of the black curve to compensate for the spectral centroid offset (red line).

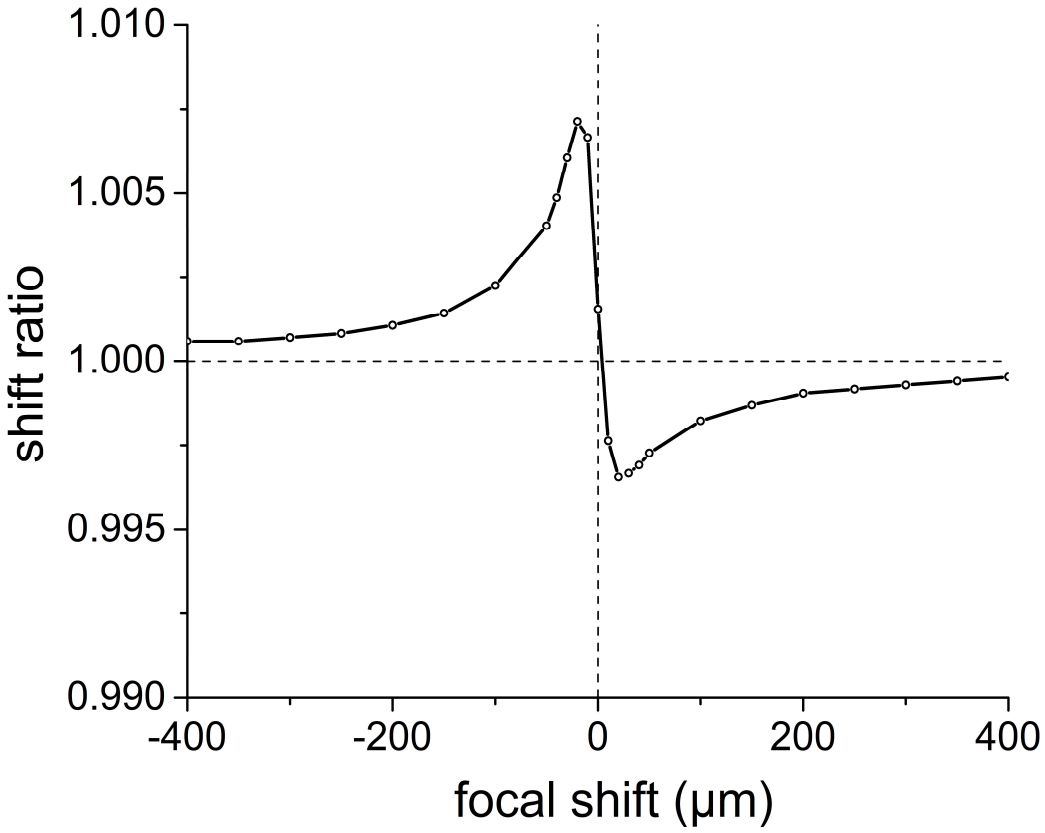

Figure S13. Estimation of spectral centroid shift due to chromatic focal shift using Zemax simulation, related to Figure 2B, 2E, 3D, 4B, 4E, 5C and 5D.

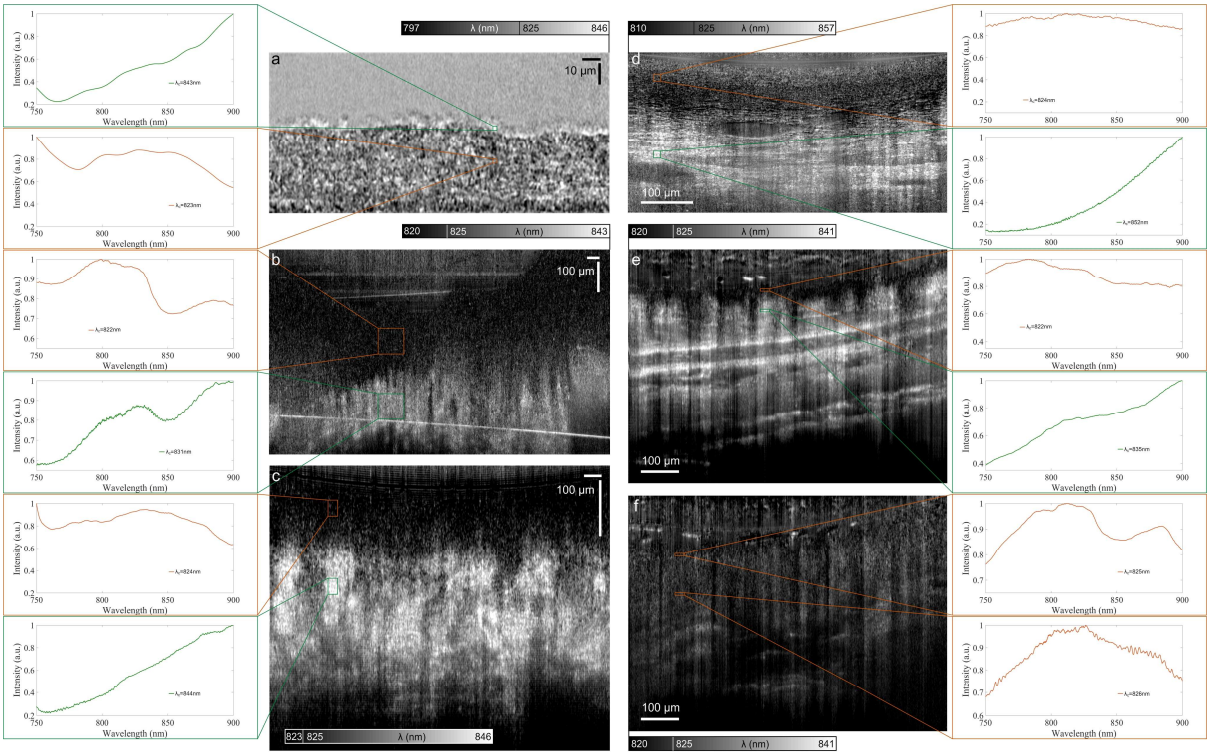

Figure S14. Corresponding spectral curves range from 750-900 nm of different types of tissue, related to Figure 2B, 3D, S4, S5, 4B and 4E. (a) motile cilia in HBE culture, (b) swine optic nerve head, (c) human skin from the volunteer with medium skin pigmentation, (d) swine oesophagus, (e) normal mouse ear skin and (f) burned mouse ear skin.

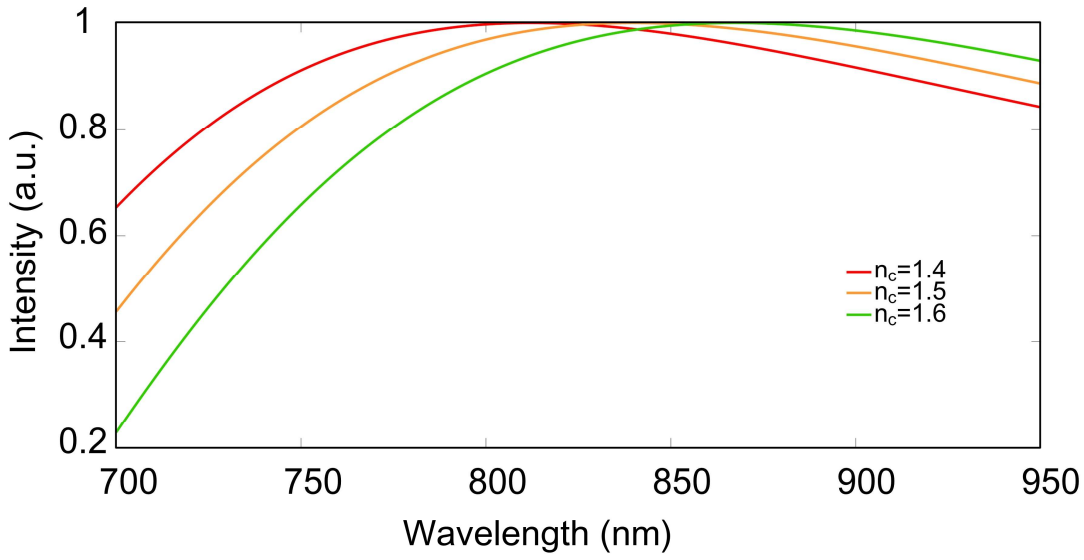

Figure S15. Effect of refractive index variations in a representative model of Figure S7c with a radius of 40 nm and d_c=0.5, related to Figure 3A. Each curve was normalized to its peak.

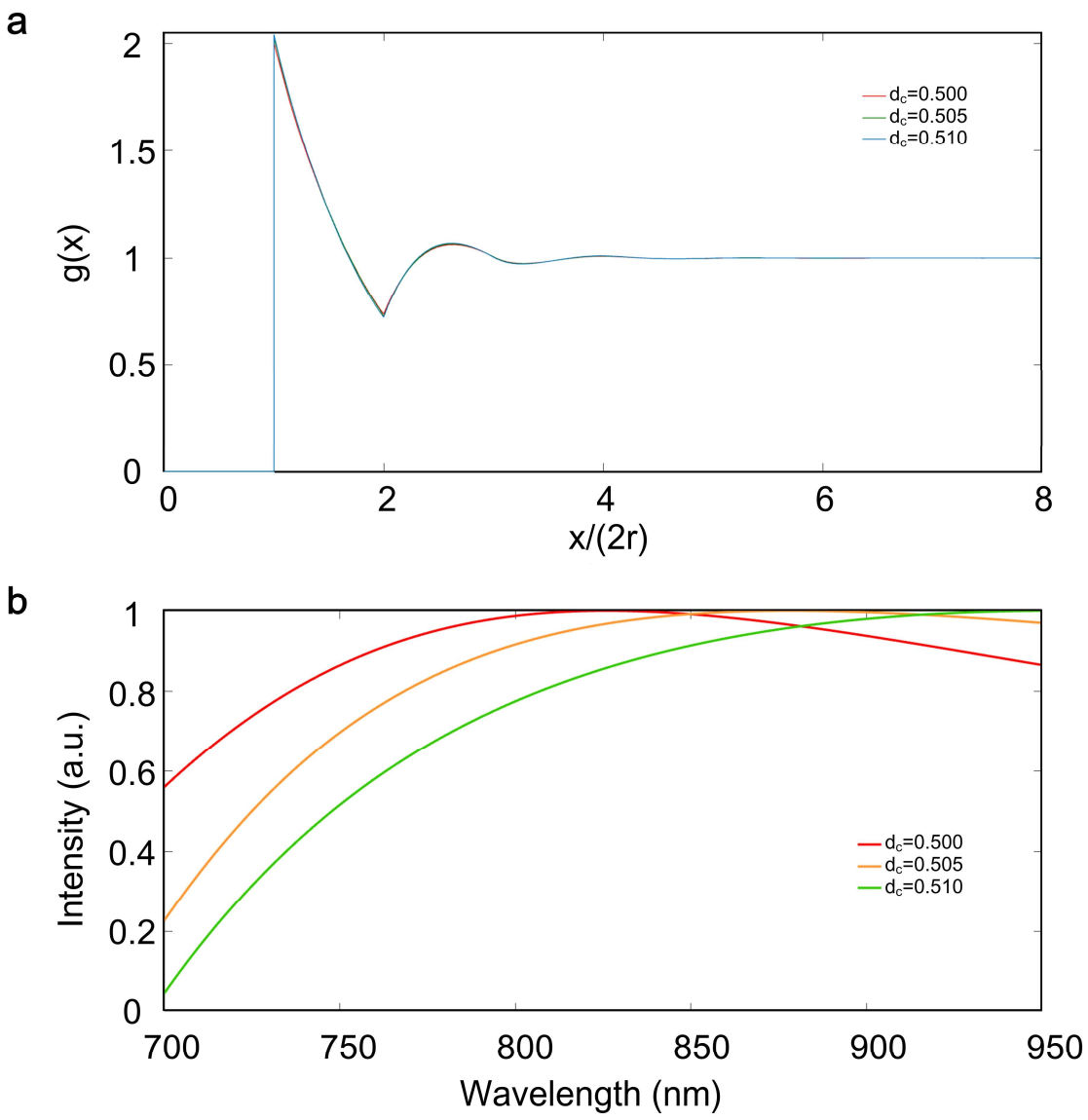

Figure S16. (a) Radial distribution function g(x) for values of d_c. (b) Backscattered spectrum varies as g(x) and d_c. Spectral curve was normalized to its peak. This is related to **Figure 3A**.

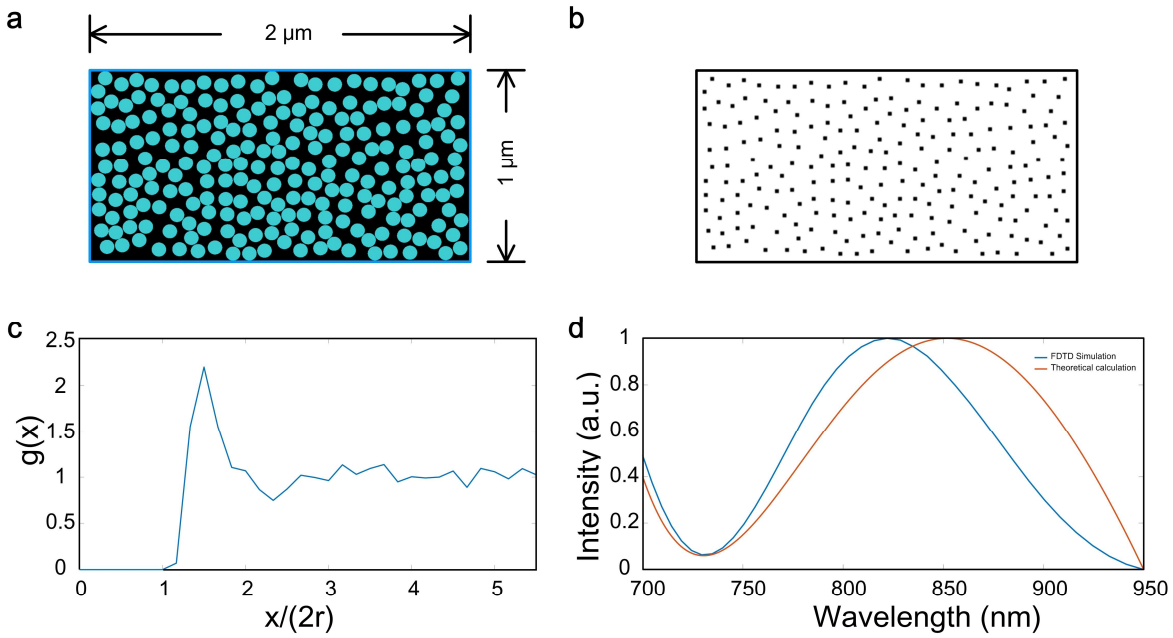

Figure S17. FDTD simulation and theoretical calculation for a representative random packing nano-cylinders, related to Figure 3A. (a) The cyan disks indicate the cross section of cylinders with a radius of 40 nm. (b-c) Center-points of nano-cylinders used for the calculation of radial distribution function g(x). (d) Plots of the backscattered spectra, result from FDTD simulation in the blue line and the theoretical calculation in the red line.

Supplemental Tables

Optical parameters/structural parameters	**Value**	
Sources	Gaussian wave	
Collected N.A.	0.2	
Wavelength (nm)	700-950	
Polarization	unpolarized	
Refractive index of cilia (Welch et al., 2005)	1.57, related to **Figures 1B, 1C, Figure S1 and Figure S2;** 1.4-1.6, related to **Figure S8**	
Refractive index of the surrounding medium (Schmitt and Kumar, 1998)	1.35	
	cylinders	**spheres**
Radius r (nm) (Battle et al., 2015)	100	100
Spacing distance D (centre to centre) (Rhodin, 1966)	>3r	>3r
Structure volume (μm × μm × μm)	2 (x)× 2 (y)× 2 (z)	2 (x)× 2 (y)× 2 (z)

Table S1. Optical and structural parameters for FDTD modelling (motile cilia and spherical scatterer model), related to Figure 1B and 1C.

Optical parameters/structural parameters	**Value**	
Sources	Gaussian wave	
Collected N.A.	0.2	
Wavelength (nm)	700-950	
Polarization	unpolarized	
Refractive index of collagen fibril (Bashkatov et al., 2000; Wang et al., 1996)	1.45	
Refractive index of the surrounding medium (Schmitt and Kumar, 1998)	1.35	
	well-aligned	**mis-aligned**
Radius (Quigley et al., 1991) r (nm)	30-50, random distribution	30-50, random distribution
Spacing distance D (centre to centre) (Quigley et al., 1991)	$>r_1+r_2$	$>r_1+r_2$
Structure volume (μm × μm × μm)	2 (x)× 2 (y)× 1 (z)	2 (x)× 2 (y)× 1 (z)

Well-aligned: cylinders have the same direction in y direction, but are disordered in the x-z plane.
Mis-aligned: cylinders have the random direction in y direction, with the same distribution as the well-aligned case in the x-z plane.
r_1 and r_2: the radii of adjacent nano-structures.

Table S2. Optical and structural parameters for FDTD modelling (collagen fibril model), related to Figure 3A and 3B.

Figure	Averaging frames	**Video**	Averaging frames
2A, 2B, 2C and S14a	50	**S1**	1
2D, 2E, 2F	10	**S2**	1
3C, 3D, 3E and S14b	10	**S3**	2
4A, 4B, 4C, 4D, 4E, 4F, S14e and S14f	50	**S4**	50
5A, 5B, 5C, 5D	50		
S4 and S14c	10		
S5a, S5b, S5c and S14d	10		

Table S3. Number of frames averaged for figures and videos, related to Figures 2-5.

Figure S7	b	c	d
Radius (r)	d_c=0.3	d_c=0.5	d_c=0.7
10 nm	805.9 nm	800.0 nm	782.6 nm
20 nm	805.6 nm	810.4 nm	820.3 nm
30 nm	805.0 nm	815.1 nm	805.5 nm
40 nm	803.6 nm	829.4 nm	879.6 nm
50 nm	801.6 nm	898.2 nm	NaN
Figure S15	n_c=1.4	n_c=1.5	n_c=1.6
40 nm	826.8 nm	832.5 nm	840.1 nm
Figure S16	d_c=0.500	d_c=0.505	d_c=0.510
40 nm	829.4 nm	839.5 nm	848.1 nm

Table S4. Spectral centroid of Figure S7b-d, Figure S15 and Figure S16, related to Figure 3A.

Transparent Methods

Ethics Statement

Use of human cells was approved by the Institutional Review Boards (IRB) at University of Alabama Birmingham (IRB #X080625002) and Massachusetts General Hospital (IRB #2008P000178). Primary human bronchial epithelial cells were derived from lung explants after written informed consent was obtained from subjects. The IRB at the Nanyang Technological University (IRB 2016-1-015) approved the human skin study *in vivo*, in which written informed consent was obtained from participating subjects. Institutional Animal Care and Use of Committee (IACUC) at the PWG Genetics Pte Ltd (PN16076) approved the imaging study on swine oesophagus *in vivo* and the use of discarded swine tissues. IACUC at the Nanyang Technological University (ARF-SBS/NIE-A0319) approved the use of discarded mice tissues. IACUC at the Massachusetts General Hospital (IACUC 2011N000081 and 2010N000242) approved the use of discarded sheep tissues.

Human Bronchial Epithelial Cells

Primary human bronchial epithelial cells were derived from lung explants according to previously described methods(Rowe et al., 2010). HBE cells were cultured in 12 mm Transwell® permeable supports (Corning Inc, Corning, New York). SOCT imaging was performed on HBE cell cultures with illumination incident on the apical side of the cells. The axis of the input beam is typically placed perpendicular to the cell surface and scanned along the direction of the effective stroke or mucus transport (tangential direction of the Transwell® permeable supports).

Animal tissue imaging

We acquired tracheal tissues from a normal sheep immediately after the cessation of vital signs. The tracheal tissues were cultured in in 80 mL Ringer bicarbonate solution (KRB) baths at room temperature for 30 min prior to SOCT imaging.

For the thermal denature of collagen experiments *ex vivo*, the ears of C57BL/6 mice in week 16 were harvested after cessation of vital signs. Before each imaging experiment, one of the ears were immersed in 100°C PBS for 30 seconds while the control ear tissue was maintained at the room temperature in PBS. The ears were gently expanded using a tweezer against the optical window of the handheld probe through ultrasound transmission gel (Aquasonic 100, Vermed, Baffalo, New York, USA) before 3D OCT images were then acquired at a frame rate of 20 Hz.

For the swine coronary artery pressure loading experiment, the heart of a PWG Micropig (T-type, female, 12 months) was harvested after the cessation of vital signs. The left coronary artery was pressurized with PBS by tying the ostia to the outlet of the intravenous (IV) tubing with a suture. The pressure of the coronary artery was adjusted by manually moving the drip chamber vertically from 600 mm to 1600 mm PBS above the imaging site. We controlled the handheld probe with a 3D translation stage so that the optical window was gently in contact with the pericardium above the coronary artery. The cross-sectional OCT images of the left coronary artery were acquired through the pericardium at 20 frames per second over the entire period of pressure adjustment.

For swine oesophageal imaging *in vivo*, a PWG Micropig (T-type, female, 12 months) was anesthetized before the lumen of the oesophagus was surgically opened for the SOCT handheld probe to access the oesophageal mucosa. The oesophageal wall was expanded using sutures and the handheld probe was adjusted to be in contact with the mucosal surface through ultrasound transmission gel before the cross-sectional images were acquired at 60 frames per second.

Human Skin imaging

We conducted SOCT imaging of human forearm skin *in vivo*. The subjects were adult volunteers aged 18-40 without any skin disease history. The Fitzpatrick skin phototype of each subject was determined by

agreement between self-assessment and assessment by observers (X.W. and C.S.B.). Written consents were obtained from volunteers before image acquisition. During the image acquisition, the forearm skin was in contact with the optical window mounted around the focal plane of the handheld probe. The ultrasound transmission gel was used to avoid surface reflections. A gentle pressure was applied on the optical window to expand the skin when 3D images were acquired at 60 frames per second with 1024 axial scans/second and each dataset within 17 seconds. The optical power incident on the mucosa was 1.8 mW.

SOCT device and signal processing

SOCT is an extension of optical coherence tomography (OCT). The construction of OCT imaging system has been reported previously (Chen et al., 2017) (**Figure S10**). In brief, a supercontinuum light source (SC-5, Yangtze SotonLaser, Wuhan, China) provided a broadband illumination from 700 to 950 nm. The output from the light source was split by a 50:50 beamsplitter to the sample arm and the reference arm. The light beam in the sample arm passed through a collimation lens (AC050-015-B-ML, Thorlabs, Newton, USA) and a galvo scanner (GVSM002/M, Thorlabs, Newton, USA) and was focused by an objective lens (M Plan Apo NIR 20×, Mitutoyo, Takatsuku, Japan). The light beam in the reference arm was reflected from a reference mirror back to the fibre coupler and interfered with the light beam reflected from the sample. Finally, the interfered light was recorded by a spectrometer consisting of a collimation lens (AC127-030-B-ML, Thorlabs, Newton, USA), a diffraction grating (1200 l/mm @ 840 nm, Wasatch Photonics, Logan, USA), a camera lens (AF Nikkor 85 mm f/1.8D, Nikon, Tokyo, Japan), and a high-speed line CCD camera (AViiVA EM4, e2v, Chelmsford, UK). The backscattered spectrum of each voxel in the 3D dataset was obtained by use of short-frequency Fourier transform (SFFT). A moving window Δk of 0.46 μm^{-1} ($\Delta\lambda$=50nm at 825nm) is applied to the fast Fourier transforms (FFTs) of the interferometric data with a degraded axial resolution around 6 μm in air. The window is moved in steps of 0.25 nm. Due to the low spectral resolution, it is inaccurate to fit the measured spectra that we chose the spectral centroid as the spectroscopic metric.

Finite-difference time-domain simulations

We carried out a numerical simulation of packed nanometre-scale scatterers using the finite-difference time-domain (FDTD) method (Lumerical FDTD Solutions, Vancouver, Canada) and scalar diffraction theory (Liu et al., 2005). To access the spectral centroid shift of packed nanometre-scale scatterers, a micrometre-scale focal volume composed of absorption-free structures was generated with well-defined perfectly matching layer (PML) boundaries and a finite-sized mesh. Nanometre-scale scatterers with a uniform radius r were constructed via the modified simple sequential inhibition (SSI) method (Bagi, 2005). Sixty-four layers of PML boundaries, which absorbed light radiation with minimal reflection, were set. The mesh size was one-tenth of the radius r, which guaranteed the absorption of sufficient light waves with minimal reflections and sampling accuracy. Non-overlapping scatterers were randomly distributed in the surrounding medium with a refractive index n_m=1.35. A new scatterer was sequentially placed with a minimum distance D from edge to edge until no more scatterers could be placed inside (**Figure S11a**). Once a new scatterer intersected a previous scatterer or PML, it would be rejected, and the next scatterer would be tested. The light was scattered by discontinuities in the refractive index within the selected volume. The typical parameters for the cilia model and collagen fibril model are listed in **Tables S1** and **S2**, respectively.

The backscattered spectral signal of the selected volume in the sample arm of SOCT was acquired through four subprocesses: the injection of the Gaussian beam, light interaction with the scatterers, near-field to far-field transformation and far-field propagation to the tip of the optical fibre (**Figure S11b**). The incident beams were unpolarized by incoherently summing results from beams with a polarization angle from 0° to 360°. The sampling interval of the polarization angle was uniform and set to 20°. Next, an optical field monitor was placed immediately behind the packed nanoscale scatterers to collect the backscattered near field. Cylindrical scatterers were assumed to be oriented and aligned in a lateral plane perpendicular to the direction of the incident light. The electric field collected from the scatterers was projected onto an image plane according to the scalar diffraction theory. Consequently, the spectral centroid shift the light scattered from the packed nanometre-scale scatterers with respect to that of the incident light could be obtained.

Specifically, the incident light beam U_i was assumed to be a Gaussian wave with a quasi-rectangular power spectrum:

$$U_i(\lambda, x, y, z) = U_0(\lambda, z)\exp\left[\frac{-\left(x^2 + y^2\right)}{w(z)^2}\right] \tag{1}$$

where λ is the wavelength of the light beam, x-, y- and z- position is determined from the focus of the beam, and $w(z)$ is spot size with the distance z from the beam waist that is set at z=0.

The backscattering field near the scatterers is $U_{near}(\lambda)$, which is corrected by the reduction of any diffraction errors caused by the Gaussian source:

$$U_i(\lambda) \overset{FDTD}{\rightarrow} U_{near}(\lambda) \tag{2}$$

Next, the intensity of the electric field in the far field was collected by the 4-f system and propagated to a detection pinhole based on the scalar diffraction theory:

$$I_{far}(\lambda) = \left|U_{far}(\lambda)\right|^2 = \left|\Im\left(\Im\left(U_{near}(\lambda)\right)\cdot P\right)\right|^2 \tag{3}$$

where $\Im$ denotes the Fourier transform, and P is the pupil function.

Under the conditions of Gaussian approximation for a single-mode fibre, the output spot, I_s, obeys a Gaussian distribution (Gu et al., 1991):

$$I_s(\lambda) = I_{far}(\lambda)\cdot\left(\exp\left(-l^2/2l_0^2\right)\right)^2 \tag{4}$$

where l is the distance from the center of the fibre, and l_0 is the spot size.

Finally, the spectral centroid λ_c was calculated as follows:

$$\lambda_c = \frac{\int_{\lambda_1}^{\lambda_2} I_s(\lambda)\lambda d\lambda}{\int_{\lambda_1}^{\lambda_2} I_s(\lambda) d\lambda} \tag{5}$$

where λ_1 and λ_2 are the minimum and maximum value of the wavelength.

Calibration for the undersampled spectral interferogram

In Fourier Domain-OCT, the OCT intensity image can be reconstructed via the Fourier transform of the interferogram:

$$I_{\mu OCT}(z) = 2\int_{-\infty}^{\infty}\sqrt{I_r(k)I_s(k)}\cos(2kz)\exp(-ikz)dk \tag{6}$$

where $I_r(k)$ and $I_s(k)$ are the intensity reflectivity, z is the depth in the sample space, and k is the wavenumber. A short-frequency Fourier transform of the interferogram can be expressed as follows:

$$S_{\mu OCT}(k, z) = 2\int_{-\infty}^{\infty}\sqrt{I_r(k')I_s(k')}\cos(2k'z)w(k' - k; \Delta k)\exp(-ik'z)dk' \tag{7}$$

where w is a window function that is a rectangular window with width Δk centred at k.

The number of cycles in the interferogram is determined by z/L_c, where $L_c=\lambda^2/\Delta\lambda$ is the coherence length of the light source. Due to the wavenumber-space nonlinearity of the spectrometer, the signal from the short wavenumber light will decay faster than the long wavenumber light over depth, causing an error in the centre of gravity of the spectrum.

To quantify and correct the spectral centroid offset due to wavenumber-space nonlinearity, we placed a mirror in the sample arm while a reference mirror was fixed. Moving the sample mirror along the direction of depth enabled measurement of the centre of gravity of the spectrum at each depth. The fitting curve in **Figure S12** was normalized by the central pixel number of the camera in the spectrometer. Final data sets were calibrated by the fitting function to compensate for spectral centroid offset.

Chromatic aberration, light transport and noise correction

In OCT system, the backscattered intensity at the depth z can be expressed as,

$$I(z,\lambda) = I_0 \frac{L_c \mu_b(z,\lambda) A(z,\lambda)}{2} \int_0^z \exp(-2\mu_s(z,\lambda)\bar{n}z')dz' \quad (8)$$

where I_0 is the illumination intensity, L_c is the coherence length, and $\bar{n}$ is the mean refractive index of tissues. $\mu_b(z,\lambda)$ is the desired variable affected by the local scatterer geometry. $A(z,\lambda)$ is the beam divergence function result in chromatic focal shift. $\mu_s(z,\lambda)$ is the scattering coefficient depended on the optical properties of tissues.

To determine the influence of chromatic focal shift on the spectral centroid, we built an aberration analysis model in Zemax (LLC, Washington, USA). The Zemax model was constructed based on the parameters of our experimental setup. Rays of different wavelengths were weighted in terms of the spectral distribution of the light source. In the sample arm, the single-mode fibre (780 HP, Thorlabs, Newton, USA) output light was a diverging beam with numerical aperture NA=0.13. Through the collimation lens with f=15 mm and focusing lens with f=10 mm, a spot diagram of all rays could be traced in and out of the diffraction-limited region, where the focus plane was placed at z=0, and z takes positive values on the right-hand side of the focal plane. The spectral centroid of the different axial positions could be calculated by the RMS spot radius and Strehl ratio, as shown in **Figure S13.** A relative shift ratio of below 1% is considered acceptable.

In practice, the measurements of $\mu_s(z,\lambda)$ are technically challenging in OCT system as the integral in $\mu_s(z,\lambda)$ is over all angles and $\mu_s(z,\lambda)$ is hard to quantified along the penetration depth. Any approximation of $\mu_s(z,\lambda)$ is inappropriate and corresponding compensation may result in a degraded accuracy of spectroscopic signals. In this work, $\mu_s(z,\lambda)$ is assumed as wavelength independent when the probing depth is not large enough. Moreover, based on the Beer's law in Eq. (8), illumination is attenuated by the integral of the penetration depth. As the cumulative effect of scattering attenuation, even $\mu_s(z,\lambda)$ is wavelength dependent, it could only alter the spectrum gradually, but not conversely as we observed (**Figure S14**).

Not like other denoising methods such as wavelet transform based filters or bandpass filters applied to spectrum, we cut off the edges of spectrum (20-30 nm away from its edge), where the noise may dominate (Oldenburg et al., 2007). In the spectral analysis, the spectral interferogram was normalized to the illumination spectrum ranges from 750 nm to 900 nm. In addition, frame averaging is used to smooth the spectral response of speckles.

Backscattered theory of packed cylinders

To quantify the spectral centroid shift of a subject with discontinuous structure on the nanoscale, detailed analysis of the size and spatial distribution of nano-cylinders has been carried out. Since $\mu_a << \mu_s$ with NIR light in biological tissues, the extinction coefficient $\mu_t \cong \mu_s$ where μ_a and μ_s are the absorption and

scattering coefficients, respectively. Here, we considered the localized backscattering coefficient μ_b sensitive to the geometry of nano-cylinders with a thickness Δz of 1-2 μm, through which the intensity of OCT image at the depth of z+Δz is defined by (Schmitt et al., 1993)

$$\begin{aligned} I(z+\Delta z) &= I(z)\frac{L_c\mu_b(z+\Delta z)}{2}\int_0^{\Delta z}\exp(-2\mu_s\bar{n}\Delta z)dz \\ &= I(z)\frac{L_c\mu_b(z+\Delta z)}{4\mu_s}\left[1-\exp(-2\mu_s\bar{n}\Delta z)\right] \\ &\approx I(z)\frac{L_c}{2}\mu_b(z+\Delta z)\Delta z\bar{n} \quad \text{for} \quad \Delta z << 1/\mu_s \end{aligned} \tag{9}$$

where $\bar{n}$ is the refractive index of tissue and L_c is the coherence length of the light source. As the thickness of cylinders array Δz is largely smaller than the scattering mean free path $1/\mu_s$, around 0.1-1 mm in the biological tissue (Schmitt et al., 1993), then the exponential term could be approximated in Eq. (9). It is worth noting the reflection and refraction at the interface between z and z+Δz are eliminated, since the mismatch of refractive index are treated as wavelength independent. In SOCT, the spectrum of μ_b could be acquired by the SFFT processing (Yi and Backman, 2012). To derive the mathematical expression of μ_b, we developed the Hart and Farrell approach (Hart and Farrell, 1969), which employs the radial distribution function g(x) to describe the scattering properties of nanometre-scale cylinders array. For a transversely oriented and parallel arrangement of noninteracting nano-cylinders with identical radius r, μ_b can be estimated as the product $\rho\sigma$, where $\rho = d_c/\pi r^2$ is the number density of cylinders, d_c is the cross-sectional packing fraction, σ is the backscattering cross section for the nano-cylinders assembly. By integrating over the angles θ, and backscattered coefficient may be written as

$$\begin{aligned} \mu_b &= \rho\int_{\pi-\theta_{max}}^{\pi+\theta_{max}}\sigma(\theta)d\theta \\ &= \rho\int_{\pi-\theta_{max}}^{\pi+\theta_{max}}\sigma_0(\theta)\{1+2\pi\rho\int_0^L x dx\left[g(x)-1\right]J_0\left[2kx\sin(\frac{\theta}{2})\right]\}d\theta \end{aligned} \tag{10}$$

Here $\sin\theta_{max} = \text{N.A.}$ is the numerical aperture of the objective. The first term of Eq. (10) is the scattering cross section of the individual cylinder and the second term of Eq. (10) takes into account the interference effects. The scattering calculation can be simplified by approximating the scattering angle is π,

$$\sigma(\pi) = \sigma_0(\pi)\{1+\alpha(\pi)2\pi\rho\int_0^L x dx\left[g(x)-1\right]J_0(2kx)\} \tag{11a}$$

when the incident light is unpolarized,

$$\sigma_0(\pi) = \frac{|F_1(\pi)|^2 + |F_2(\pi)|^2}{\pi k} \tag{11b}$$

with

$$|F_1(\pi)|^2 = (\frac{kr}{2})^4\pi^2(m^2-1)^2\{1-2(\frac{kr}{2})^2\left[2(m^2-1)\ln(\frac{\gamma kr}{2})+\frac{3-m^2}{2}\right]\} \tag{11c}$$

and

$$|F_2(\pi)|^2 = (\frac{kr}{2})^4 \frac{2\pi^2(m^2-1)^2}{(m^2+1)^2}\{1-\frac{2}{m^2+1}(\frac{kr}{2})^2\left[2(m^2-1)\ln(\frac{\gamma kr}{2})+\frac{3+m^2}{2}\right]\} \quad (11d)$$

When Eqs. (11c) and (11d) are substituted into Eq. (11b), we could obtain the final expression for $\sigma_0(\pi)$ and μ_b ,

$$\sigma_0(\pi) = \frac{\pi k^3 r^4}{16}(m^2-1)^2\{1+\frac{2}{(m^2+1)^2}-k^2r^2(m^2-1)\ln(\frac{\gamma kr}{2})\left[1+\frac{2}{(m^2+1)^3}\right]-\frac{k^2r^2}{4}\left[3-m^2+\frac{2(3+m^2)}{(m^2+1)^3}\right]\} \quad (12)$$

$$\mu_b = \frac{d_c}{\pi r^2}\sigma_0(\pi)\{1+2\pi\rho\int_0^L x dx\left[g(x)-1\right]J_0(2\bar{k}x)\} \quad (13)$$

where $k = 2\pi n_m/\lambda$, $\bar{k} = 2\pi\bar{n}/\lambda$, λ is the wavelength in the vacuum, $m = n_c/n_m$ is the ratio of the refractive index (RI) of the nano-cylinders n_c to that of the surrounding medium n_m, average RI $\bar{n} = d_c n_c + (1-d_c)n_m = n_m\left[d_c(m-1)\right]$, $\bar{n}L$ is the optical path difference, $\ln\gamma$ is the Euler constant that $\gamma \cong 1.78$, g(x) equals to 1 for $L > L_R$, L_R is the correlation distance, and J_0 is the Bessel function of the first kind of order zero. It is important to note that Eq. (11c) and Eq. (11d) are valid when the radius of nano-cylinders r is much smaller than the wavelength. For larger cylinder radius such as that of cilia, the full expression of Eq. (11c) and Eq. (11d) should be adopted as in (Hart and Farrell, 1969). Eq. (13) therefore shows that the backscattered spectrum depends on the cylindrical radius r, the ratio of the refractive indices m, and the radial distribution function g(x), that would be evaluated numerically for each case of interest.

First, we used the radial distribution function g(x) to describe the interference by the scattered fields from two nano-cylinders, separated by an optical path difference $\bar{n}L$ that in terms of x/(2r). In accordance with the approach of A. Santos (Santos, 2012), the radial distribution function (**Figure S7a**) of simple hard cylinders with zero stickiness was generated, characterized by the packing fraction d_c. Then the backscattered spectra is related directly to g(x) and can vary from d_c=0.3 (**Figure S7b**), d_c=0.5 (**Figure S7c**), to d_c=0.7 (**Figure S7d**). Here, m is set to 1.45/1.35≈1.07, and r is varied from 10 nm to 50 nm. The calculated spectra in **Figure S13b** shows that the backscattered intensity decreases with the wavelength for d_c=0.3. Interestingly, some of the long-wavelength shifting tendency happens for d_c=0.5 and d_c=0.7. The results clearly indicate that the existence of long-wavelength shifting spectra for nano-cylinders and that backscattered light could interfere constructively and destructively. It should be mentioned that some of the intensity values over the wavelength are forced to zero when they are negative. The zero values of backscattered intensity are not meaningful but indicate strong destructive interference. Second, we considered the changes in the backscattered spectrum described only by the reflective index (RI) of the nano-cylinders n_c. Parameters correspond to the purple line in **Figure S7c**, in addition to n_c varied from 1.4 to 1.6. The behaviour of the spectral shifts (**Figure S15**) is similar to the FDTD result plotted in **Figure S8**. Last, we turned to investigate the role of spatial distribution of nano-cylinders characterized by the radial distribution function g(x) depended on the packing factor d_c, which is a key unknown in the spectral shift. Parameters also are chosen as those of the purple line in **Figure S7c**, but with different values of d_c. **Figure S16b** illustrates the peak of spectral shifts to the long-wavelength as the d_c increases. The sensitive spectral movement due to the change of a step of 0.005 in d_c implies that the couple of d_c and g(x) should be an important factor to spectral shifts.

Taking a representative case for example, the cross-section view (**Figure S17a)** of the closely packed nano-cylinders is adapted from one of our FDTD models. Nano-cylinders are placed at a random position and cannot approach closer than touching. The radius of nano-cylinders is 40 nm, m is set to 1.07, and the packing fraction is the area occupied by the nano-cyliders divided by the entire area, which is

$\frac{223 \times \pi \times (40e^{-9})^2}{2e^{-6} \times 1e^{-6}} = 0.56$. The spatial coordinates of nano-cylinders' centers in **Figure S17b** are used to calculate the radial distribution function g(x) (**Figure S17c**). Different from the approach above, g(x) here is calculated from a specific model, which is independent with d_c. Interestingly, the theoretical calculation is in close agreement with the FDTD simulation (**Figure S17d**) when the interference term (the second term of Eq. (13)) is half of the individual term (The first term of Eq. (13)). Therefore, the equation for the theoretical calculation in **Figure S17d** is,

$$\mu_b = \frac{d_c}{\pi r^2}\sigma_0(\pi)\{1 + \pi\rho\int_0^L x dx\left[g(x) - 1\right]J_0(2\bar{k}x)\} \quad (14)$$

This happened probably because we assumed θ_{max} is small, did not account for the angle integration and considered only $\theta = \pi$.

Data and image processing tools

All the data post-processing was implemented in MATLAB (MathWorks, Natick, USA). OCT and SOCT volumes were saved as bmp stacks. **Video S1 and S4** were made with ImageJ (https://imagej.nih.gov/ij/). **Videos S2** and **S3** were made with Avizo 9 (FEI Visualization Science Group, Hillsboro, USA).

All image analysis was performed with ImageJ (https://imagej.nih.gov/ij/) and MATLAB (MathWorks, Natick, USA).

References

Bagi, K. (2005). An algorithm to generate random dense arrangements for discrete element simulations of granular assemblies. Granular Matter *7*, 31-43.

Bashkatov, A.N., Genina, E.A., Kochubey, V.I., and Tuchin, V.V. (2000). Estimation of wavelength dependence of refractive index of collagen fibers of scleral tissue. Paper presented at: Controlling Tissue Optical Properties: Applications in Clinical Study (International Society for Optics and Photonics).

Battle, C., Ott, C.M., Burnette, D.T., Lippincott-Schwartz, J., and Schmidt, C.F. (2015). Intracellular and extracellular forces drive primary cilia movement. Proceedings of the National Academy of Sciences *112*, 1410-1415.

Chen, S., Liu, X., Wang, N., Wang, X., Xiong, Q., Bo, E., Yu, X., Chen, S., and Liu, L. (2017). Visualizing Micro-anatomical Structures of the Posterior Cornea with Micro-optical Coherence Tomography. Scientific reports *7*, 10752.

Gu, M., Sheppard, C., and Gan, X. (1991). Image formation in a fiber-optical confocal scanning microscope. JOSA A *8*, 1755-1761.

Liu, Y., Li, X., Kim, Y.L., and Backman, V. (2005). Elastic backscattering spectroscopic microscopy. Optics letters *30*, 2445-2447.

Rhodin, J.A. (1966). Ultrastructure and function of the human tracheal mucosa. American Review of Respiratory Disease *93*, 1-15.

Rowe, S., Pyle, L., Jurkevante, A., Varga, K., Collawn, J., Sloane, P., Woodworth, B., Mazur, M., Fulton, J., and Fan, L. (2010). ΔF508 CFTR processing correction and activity in polarized airway and non-airway cell monolayers. Pulmonary pharmacology & therapeutics *23*, 268-278.

Schmitt, J., Knüttel, A., and Bonner, R. (1993). Measurement of optical properties of biological tissues by low-coherence reflectometry. Applied Optics *32*, 6032-6042.

Wang, X.-j., Milner, T.E., Chang, M.C., and Nelson, J.S. (1996). Group refractive index measurement of dry and hydrated type I collagen films using optical low-coherence reflectometry. Journal of biomedical optics *1*, 212-217.

Welch, V., Vigneron, J., and Parker, A. (2005). The cause of colouration in the ctenophore Beroe cucumis. Current Biology *15*, R985-R986.